LOW-FREQUENCY BULK AND SURFACE GENERATION-RECOMBINATION NOISE SIMULATIONS OF SEMICONDUCTOR DEVICES

By

FAN-CHI (FRANK) HOU

A DISSERTATION PRESENTED TO THE GRADUATE SCHOOL
OF THE UNIVERSITY OF FLORIDA IN PARTIAL FULFILLMENT
OF THE REQUIREMENTS FOR THE DEGREE OF
DOCTOR OF PHILOSOPHY

UNIVERSITY OF FLORIDA

2002

Copyright 2002

by

Fan-Chi (Frank) Hou

I dedicate this work to all of my friends and family who have supported my efforts over the years and believed in me.

ACKNOWLEDGMENTS

I would like to express my sincere gratitude to Dr. Gijs Bosman for the support, encouragement and guidance he gave me for this project. I would also like to thank Dr. M. Law, Dr. R. Fox, Dr. O, and Dr. Stanton for serving on my committee. In addition, I appreciate the financial and technical support from the Semiconductor Research Corporation; and I thank Dr. Donald Hemmenway (Intersil) and Dr. Rainer Thoma (Motorola) for providing simulation profiles and data.

Finally, I would like to thank my wife and my parents for their love and support over the years.

TABLE OF CONTENTS

page

ACKNOWLEDGMENTS iv

LIST OF FIGURES vii

ABSTRACT xi

CHAPTER

1 INTRODUCTION 1

- 1.1 Noise Sources in Semiconductor Devices 1
- 1.2 PDE-Based Device and Noise Simulator 2
  - 1.2.1 Theory of Noise Simulation 4
  - 1.2.2 Velocity-Fluctuation Noise Examples 6
- 1.3 Organization and Overview 8

2 BULK GENERATION-RECOMBINATION NOISE 25

- 2.1 Introduction 25
- 2.2 Theory 26
- 2.3 "Indirect" Approach 28
- 2.4 "Direct" Approach 31
- 2.5 Simulation Verification 31

3 INTERFACE GENERATION-RECOMBINATION NOISE 49

- 3.1 Introduction 49
- 3.2 Theory 49
- 3.3 DC and Noise Simulations 51
- 3.4 Simulation Results 54

4 OXIDE TRAPPING NOISE 63

- 4.1 Introduction 63
- 4.2 Theory and Implementation 64
  - 4.2.1 "Capture and Tunneling" Model 65
  - 4.2.2 Modeling of the Defect Density in Oxide 67
  - 4.2.3 Modeling of the Carrier Tunneling Rates 69
- 4.3 Verification with Analytical Expressions 70
- 4.4 Noise Spectroscopy 73

4.5 Summary 76

5 MAXIMUM ALLOWABLE BULK DEFECT DENSITY FOR GENERATION-RECOMBINATION NOISE FREE OPERATION OF n^+-n-n^+ STRUCTURES 91

5.1 Introduction 91
5.2 Implementation 92
5.3 Simulation 94
5.4 Discussion 97
5.5 Conclusions 98

6 CONCLUSION AND SUGGESTIONS FOR FUTURE RESEARCH 108

REFERENCES 110

BIOGRAPHICAL SKETCH 113

LIST OF FIGURES

Figure page

1-1 Different types of noise observed in a noise experiment 11

1-2 Low-frequency 1/f-like noise produced from a superposition of Lorentzian spectra, caused by the g-r mechanism 12

1-3 Local g-r noise strength to the external contact through the scalar Green's function 13

1-4 Doping profile of a pn diode. The emitter region with a peak acceptor concentration of $5 \cdot 10^{17}$ cm^{-3} is implanted in a uniformly doped base substrate with a 10^{15} cm^{-3} donor concentration. 14

1-5 Current noise spectral density vs. diode voltage. The analytical and simulation results are compared. Note that the analytical result is only valid under low injection conditions. 15

1-6 Distributed current noise spectral density for both carriers, under low injection conditions (V_{diode} = 0.4 V) 16

1-7 Distributed current noise spectral density for both carriers, under high injection conditions (V_{diode} = 1.4 V) 17

1-8 Doping profile of a npn BJT structure 18

1-9 Current noise spectral density vs. bias current. The collector is biased at 1.0 V, while the base is swept from 0.3 to 0.7 V. (a) Noise at the base terminal. (b) Noise at the collector terminal. 19

1-10 Distributed current noise spectral density at the base contact under low injection condition (V_{ce} = 1.0 V, V_{be} = 0.5 V). (a) Electron component. (b) Hole component. 20

1-11 Distributed current noise spectral density at the collector contact under low injection condition (V_{ce} = 1.0 V, V_{be} = 0.5 V). (a) Electron component. (b) Hole component. 21

1-12 Doping profile of a n-channel MOSFET. The channel length is about 2 μm. 22

1-13 Current noise spectral density vs. drain bias voltage (V_{gs} = 1.5 V) 23

1-14 Distributed current noise spectral density contributions at the drain contact (V_{ds} = 1.5 V, V_{gs} = 0.4 V). (a) Electron component. (b) Hole component. 24

2-1 Carrier transitions between the continuum states and localized defect states 38

2-2 Comparison between the simulated and analytical current noise spectral density as a function of frequency. The bias across the device is set to 0.1 V. 39

2-3 Bulk g-r noise simulated as a function of trap energy level (f = 1 Hz) . . 40

2-4 Fermi and g-r trap energy levels. The energy levels of g-r traps are represented by the dashed lines, and the position of the Fermi level is shown by the solid line. 41

2-5 Low frequency g-r noise plateau $S_v(0)/V_o^2$ versus $1000/T$ 42

2-6 Characteristic time τ_t of different traps versus $1000/T$ 43

2-7 Noise from different bulk g-r trap centers 44

2-8 Distributed current noise spectral density (f = 1 Hz) of the MOS structure operating in the triode mode of operation (V_{gs} = 1.5 V, V_{ds} = 0.3 V, and V_t = 0.932 V) 45

2-9 Noise simulated with different capture coefficients 46

2-10 Noise with different capture coefficients plotted as a function of frequency 47

2-11 Noise simulated with different defect densities 48

3-1 Measured trap density distribution from the conductance method [14] . . . 56

3-2 Energy band diagram at the interface, with the presence of a discretized trap energy level at E_f 57

3-3 Trapped carriers at non-discretized trap levels induce a charge Q_{itf} at the interface 58

3-4 Interface trap carrier density $n_{t,itf}$(marked by "x") and interface charge Q_{itf}/q (marked by "o") for a V_{gs} sweep (V_{ds} and V_{bs} are set to zero) . . . 59

3-5 Interface trap carrier density $n_{t,itf}$ for a V_{ds} sweep. V_{gs} is set to a value greater than V_t and V_{bs} is set to zero. 60

3-6 Distributed interface current noise spectral density for different V_{ds}. V_{gs} is set to a value greater than V_t and V_{bs} is set to zero. 61

3-7 Various current noise spectral densities for a V_{gs} sweep (V_{ds} = 1.0 V) . . . 62

4-1 "Tunneling and Capture" and "Capture and Tunneling" models 77

4-2 Simulation results are plotted and compared with the analytical prediction. 78

4-3 Current noise spectral density vs. frequency 79

4-4 Distributed current noise spectral density for different frequencies 80

4-5 Distributed current noise spectral density along the channel for V_{gs} = 1.0 V and V_{ds} = 0.45 V (f = 1 Hz) 81

4-6 Distributed current noise spectral density along the channel for different bias conditions 82

4-7 Device structure of a 0.45 μm graded channel MOS transistor 83

4-8 Measured current noise spectral density as a function of V_{gs} and frequency. The drain bias V_{ds} = 2.0 V. The solid lines represent the simulated background pure $1/f$ noise components. 84

4-9 Distributed current noise spectral density for f = 25 Hz. The bias values of the device under simulation are V_{ds} = 2.0 V and V_{gs} = 0.8 V. The oxide region is shown with x = 0 to be the midway between the metallurgical source and drain junctions. 85

4-10 Comparison between the simulated and measured data of the pure $1/f$ noise component (V_{ds} = 2.0 V, f = 25 Hz). 86

4-11 Profile of the defect density parameter N_0 as function of position parallel to the channel. Note that only the parameter in the oxide noise critical region indicated in Figure 4-7 is shown here. 87

4-12 Defect density profile in the smile oxide 88

4-13 Product of current noise spectral density and frequency to identify Lorentzian spectra in the measured and simulation data 89

4-14 Discrete defect distributions responsible for the Lorentzian spectra observed in the experiment. Note that only the distributions in the oxide noise critical region indicated in Figure 4-7 are shown here. 90

5-1 Carrier transitions between the continuum states and localized defect states 99

5-2 Comparison between the simulated and analytical current noise spectral density as a function of frequency. The bias across the device is set to 0.1 V 100

5-3 Comparison between the simulated and analytical g-r current noise spectral density (f = 1 Hz) as a function of the bias voltage. The dashed line represents the analytical expression (5.21). The solid line is the simulated g-r noise. The dotted line is the simulated velocity fluctuation noise. 101

5-4 Electron concentration n in the n-region as a function of position under different bias conditions. Under the low bias condition (V_{bias} = 0.1 V), $n \approx N_d$. As the bias increases ($V_{bias} > 1.0$ V), $n > N_d$. 102

5-5 Trap electron concentration n_t as a function of position under different bias conditions 103

5-6 Scalar Green's function under different bias conditions 104

5-7 Distributed current noise spectral density under different bias conditions . 105

5-8 Defect density N_{Tmax} as a function of defect energy under different bias conditions 106

5-9 I-V characteristic 107

Abstract of Dissertation Presented to the Graduate School
of the University of Florida in Partial Fulfillment of the
Requirements for the Degree of Doctor of Philosophy

LOW-FREQUENCY BULK AND SURFACE GENERATION-RECOMBINATION NOISE SIMULATIONS OF SEMICONDUCTOR DEVICES

By

Fan-Chi (Frank) Hou

May 2002

Chair: Gijs Bosman
Major Department: Electrical and Computer Engineering

Analysis of semiconductor device noise in the past has generally been separated into two parts. In the first part one tries to understand which type of noise is the dominant noise source and derive its local noise strength in each differential volume. The second part deals with deriving the transfer function, either the trans-conductance or the trans-admittance (depending on the circuit bias condition at the contact), to couple the local noise strength from each differential volume to the external contact. Integrating the product of the local noise strength and the transfer function over the device volume will produce the overall noise at the specified terminal. This type of analysis can only be done to a certain extent, since deriving the analytical expression of the transfer function is limited to only a few simple cases and device structures. To expand the capability of predicting device noise through this type of analysis, we developed a partial differential equation (PDE) -based, generalized-scheme two-dimensional semiconductor device-simulation tool to perform the transfer function calculation.

The purpose of this research is to use a computer-aided device simulation tool to analyze and simulate low frequency semiconductor device noise. To investigate the low-frequency noise, the bulk generation-recombination noise mechanism was implemented. Since this type of noise can only explain Lorentzian spectra observed in resistors but not the $1/f$-like noise in MOS devices, interface generation-recombination and the McWhorter-type oxide trapping noise mechanisms were added. The simulation results verified that oxide trapping noise (caused by the carrier fluctuations in the channel because of carrier tunneling between the trap centers in the oxide and at the interface) is indeed the source of the $1/f$ noise observed in MOS devices.

One application of this tool is noise defect spectroscopy by modeling the defect density distribution in the oxide through inverse engineering. By adjusting the defect density in the bulk and in the oxide to match the noise simulations with their corresponding measured data, one can obtain the defect density profile of the device. In addition, this tool can be used to predict the maximum amount of defects allowed to guarantee excess noise-free device operation.

CHAPTER 1
INTRODUCTION

Noise performance of today's semiconductor devices has become an important factor in the design of analog and VLSI circuits. As the devices continue to shrink in size, voltage and current signals are scaled down to accommodate the changes. Because the noise floor does not scale proportionally, the signal-to-noise ratio reduces as a result. A reduction of noise can only be achieved with better understanding of noise mechanisms and noise contributions from each physical region of the device. Once the critical regions of noise are identified, proper process steps can be applied during the manufacturing processes to lower the noise sources in those regions, in order to obtain the reduction of overall noise desired at the device terminals.

1.1 Noise Sources in Semiconductor Devices

The microscopic noise mechanisms within semiconductor devices can be classified into two categories. They are carrier velocity fluctuations and number fluctuations. Carrier velocity fluctuations are generally caused by the random scattering of carriers in the devices. Their magnitude is determined by the carrier diffusivity. They appear as a white noise, for which the noise magnitude is constant as a function of frequency, when observed in a spectral window, as shown in Figure 1-1. This mechanism becomes dominant when noise is measured at high frequencies. It also sets the lower limit of the noise at low frequencies. Examples of this type of noise mechanism are the thermal/Nyquist noise from resistive components, the shot noise in device junctions, and the diffusion noise from the channels in MOS structures.

Carrier number fluctuations are caused by random carrier transitions between continuum states and localized defect states. Fluctuations in the number of electrons and holes in the conduction and valence bands, respectively, are attributed to the trapping-detrapping of carriers to either bulk or surface defect centers. Each trap center is characterized by its energy level, trap density, and carrier capture coefficients. The trapping noise appears to be constant at low frequency, and then rolls off with a slope of $1/f^2$ when it passes its corner frequency, which is determined by the trap characteristic time, as shown in Figure 1-1. This phenomenon can be seen in resistor and JFET structures.

Low frequency $1/f$ noise is typically found in all active devices, and is also shown in Figure 1-1. There are debates on the causes of such phenomenon. One proposed by Hooge [1] suggests that it is from carrier diffusivity/mobility fluctuations due to the electron-lattice interaction, such as acoustic scattering events. Furthermore, the noise magnitude is shown not to scale significantly with impurity concentration. Measurement data obtained by the author [2] on several n^+-p gated diodes showed otherwise.

The other possible explanation of $1/f$ noise was first proposed by McWhorter [3], and assumes that superposition of a large number of Lorentzian spectra produced by generation-recombination (g-r) mechanisms would generate a $1/f$-like noise spectral density at low frequencies, as shown in Figure 1-2. Such a process can occur at the trap centers in the bulk and at the surface. Analytical derivations of this McWhorter-type g-r noise in the last half century all pointed out that this model applies well to the trapping and detrapping of carriers at the trap centers in the oxide, since only this process would have a characteristic time that is large enough to distribute Lorentzian components at low frequency.

1.2 PDE-Based Device and Noise Simulator

Partial Differential Equation (PDE), physics-based device simulators have quickly gained popularity in recent years because of their advantages over other types of device simulators and design tools. They can provide fast and accurate results. For example, they require fewer computations than Monte Carlo simulators. In addition, PDE-based device simulators are easily adapted to device model updates. Add-on software packages (such as, in our case, a noise simulator) can be created and drawn from already produced simulator parameters. Furthermore, this type of simulator can be made to extract data directly from a process simulator. This combination is a cost-effective tool for device optimization since the simulators are parameter compatible.

One of the main goals of this study was to implement known noise mechanisms into a general-purpose, multi-dimensional, PDE-based device simulation tool, and then use it to explain different noise behaviors observed in various device structures. This approach has been explored by Bonani and others [4]. His work focused on the noise mechanisms mainly observed in the bulk region of semiconductor devices, which are velocity fluctuation noise and direct band-to-band generation-recombination (g-r) noise. He later extended his focus to cover g-r noise from carrier transitions between the continuum states and the defect trap centers in the forbidden energy band-gap [5], around the same time we implemented the same mechanism to our noise simulation tool [6]. More on this topic is presented in the next chapter. As expected from the analytical theory, velocity fluctuation noise simulation results in a white noise spectrum in the spectral domain, and bulk g-r noise simulation gives a Lorentzian shape spectrum for resistor-like device structures. Neither mechanism could explain the $1/f$-like noise observed in bipolar junction transistors (BJT) or metal oxide semiconductor field-effect transistors (MOSFET). As the topic of this research states, our objective is to use noise simulation to analyze low-frequency noise in semiconductor devices, including $1/f$-like noise. In order to achieve this objective, we choose FLOODS (FLorida Object-Oriented Device Simulator), a PDE-based generalized box scheme device simulator capable of doing two-dimensional dc, ac, and transient simulations, as the tool. It was first expanded with velocity fluctuation [7] and bulk g-r noise post-processor noise capability [6], as Bonani did with the device simulator of his choice, then surface noise mechanisms were added to account for the $1/f$-like noise observed at low frequencies.

1.2.1 Theory of Noise Simulation

Noise implementation is based on the impedance field method (IFM) [8]. Two elements are required to calculate noise at the contact terminals. One is the magnitude of the microscopic noise sources at each grid point, represented by the added Langevin noise terms in the PDE equations. Depending on their physics and carrier interaction mechanisms, some noise sources, such as diffusion and bulk g-r noise sources, can be calculated using the steady-state solution of the available variables (ψ, n, p, J, μ, etc.) at each node. On the other hand, there are mechanisms, carrier tunneling for example, that require variables from nodes that are far apart to describe their dynamics and noise properties.

The other element to calculate noise is the transfer function that couples the perturbation of the PDEs from each grid point to the device terminals. This transfer function is generally called the Green's function. The Green's function for each carrier type at each node is obtained by perturbing the PDE associated with the carrier at the node, and then observing the changes at the contact terminals. Assume M is the number of PDEs in the system, and N is the number of nodes. To get the Green's functions for all the variables and all the grid points for each contact terminal, it would take ($M \times N$) matrix inversions. Bonani [4] simplifies this process by using Branin's method [9], and then it takes only one system matrix inversion to calculate the Green's function for all the nodes and PDEs in the system for a particular contact.

By implementing the noise terms to the electron and hole continuity equations as an example, we have the following PDEs

$$\frac{dn}{dt} = \frac{1}{q}\nabla \cdot (J_n + \xi_n) - U_n + \gamma_n \tag{1.1}$$

$$\frac{dp}{dt} = -\frac{1}{q}\nabla\cdot(J_p+\xi_p) - U_p + \gamma_p \tag{1.2}$$

where ξ_n ,ξ_p and γ_n ,γ_p are the Langevin noise terms for velocity fluctuation and number fluctuation noise, respectively. For the number fluctuation noise sources γ_n and γ_p , the effect is transferred to the specific contact terminal by the scalar Green's function $\tilde{G}$. For the velocity fluctuation noise ξ_n and ξ_p , the effect is through the vector Green's function $\vec{G}$, which is the gradient of the scalar Green's function, since it is the divergence of the noise source that is added to the dn/dt , dp/dt terms. The total voltage noise spectral density at the contact terminals is then calculated from integration over all noise sources [10]

$$S(\omega) = \sum_{\alpha,\beta=n,p}\int_{\Omega} \tilde{G}_\alpha \tilde{K}_{\gamma_\alpha,\gamma_\beta} \tilde{G}^*_\beta dr + \sum_{\alpha,\beta=n,p}\int_{\Omega} \vec{G}_\alpha \vec{K}_{\xi_\alpha,\xi_\beta} \vec{G}^*_\beta dr \tag{1.3}$$

where $\tilde{K}$ and $\vec{K}$ represent the microscopic noise sources for number and velocity fluctuation noise, respectively. By using the scalar Green's function already calculated by FLOODS as an example, the g-r noise spectral voltage density contact contribution from each local g-r noise source can be calculated, as shown in Figure 1-3.

The microscopic noise sources $\tilde{K}$ for number fluctuations are derived from the Poisson process and are characterized as twice the carrier transition rates. Examples are shown in subsequent chapters. The magnitude of sources $\vec{K}$ for velocity fluctuation noise, or so called diffusion noise, are given by

$$\left|\vec{K}_{\xi_n,\xi_n}\right| = 4q^2 nD_n \tag{1.4}$$

$$\left|\vec{K}_{\xi_p,\xi_p}\right| = 4q^2 pD_p \tag{1.5}$$

$$\left|\vec{K}_{\xi_n,\xi_p}\right| = \vec{K}_{\xi_p,\xi_n} = 0 \tag{1.6}$$

The velocity-fluctuation noise simulation results are shown below.

1.2.2 Velocity-Fluctuation Noise Examples

Velocity-fluctuation noise simulations were carried out with FLOODS on different semiconductor device structures. The following examples only consider the three basic PDEs for the drift-diffusion model: the Poisson, electron, and hole continuity equations. Langevin noise sources for the diffusion noise sources are specified for both the carrier continuity equations. Noise simulation results are compared with expected analytical results. As stated previously, velocity fluctuation noise is calculated from the vector Green's function, which is the gradient of the scalar Green's function. Good agreement between the simulation and the theoretical expression is crucial, since it validates both the vector and scalar Green's functions generated by the simulator.

Before proceeding to any simulation of a more complicated structure, simulations on a uniformly-doped silicon bar were first carried out. The simulated results are in good agreement with the calculated Nyquist noise

$$S_{i,diff} = 4k_B T \mathrm{Re}\{Y(f)\} \tag{1.7}$$

where $Y(f)$ is the small-signal admittance calculated from small-signal ac simulation result, k_B is Boltzmann constant, and T is the temperature.

pn Diode. Noise simulation is carried out on a 2-D diode structure. A cross-section of its doping profile between the anode and cathode is shown in Figure 1-4. In the 0.5 μm by 0.5 μm p-doped emitter region, the acceptor doping concentration is set to $5 \cdot 10^{17}$ cm^{-3}. The 3 μm by 3 μm n-doped bulk substrate is specified to have a donor doping concentration of 10^{15} cm^{-3}. In a diode structure, we expect the velocity fluctuation noise under forward bias and low-injection to show up as $2qI$, the shot noise, and then expect it to deviate from $2qI$ at high bias voltage due to high injection, where I is the diode current. The expected shot noise $2qI$ is plotted against the simulated results, and is found to be in good agreement under low injection conditions, as shown in Figure 1-5. To investigate the overall noise contribution, the distributed current noise spectral densities under low and high injection conditions are plotted in Figure 1-6 and Figure 1-7, respectively. As shown in Figure 1-6, in low injection, noise produced by the excess minority carriers dominates. As the voltage across the diode increases, noise produced by the majority carriers also increases. Noise of the diode operating in high injection is shown in Figure 1-7. In both cases, noise produced in the space charge region is not the main factor. According to Bonani [4], this phenomenon is explained by the changes in the vector Green's function. In low injection, the vector Green's functions for the majority carriers are negligible, thus the contributions by the majority carriers are minimal. As the device operation moves into high injection which causes the vector Green's functions to increase drastically, the noise contribution of the majority carriers starts to overshadow the minority contributions. This effect was confirmed by our simulation results.

npn BJT. The doping profile of a 2-D bjt structure is plotted in Figure 1-8. The n-type emitter region, p-type base region, and n-type collector substrate are uniformly-doped with doping concentrations of 10^{20} cm^{-3}, $2{\cdot}10^{17}$ cm^{-3}, and 10^{15} cm^{-3}, respectively. The emitter region is about 0.06 μm deep, and the base-collector junction is 0.5 μm below the surface. For this device structure, we expect the noise at the base and collector contacts to follow the shot noise expression, like the results we have seen in diodes. Thus we compare simulated current noise spectral densities at the base and collector contacts with $2qI_B$ and $2qI_C$, respectively. The results for low injection conditions are shown in Figure 1-9. There is good agreement between the expected and the simulated results. The distributed current noise spectral density calculated at the base contact is plotted for electrons and holes, in Figure 1-10a and 1-10b, respectively. Similar to what we obtained in the diode case, noise contributions are dominated by the minority carriers. The distributed noise spectrum, shown in

Figures 1-11a and 1-11b, shows that the majority contributions of the noise at the collector contact are from the minority carriers at the base region.

n-channel MOSFET. Noise simulation is carried out on a 2-D long channel MOSFET. Its doping profile is displayed in Figure 1-12. Both the n-type source and drain regions have a 0.25 μm deep, 10^{18} cm^{-3} donor dopant implantation. The uniformly doped p-type substrate has a 10^{17} cm^{-3} doping concentration. The diffusion current noise is expected to be $4k_BT\gamma g_{d0}$, where g_{d0} is the zero drain bias channel conductance, and for long channel devices γ varies from 1 to $2/3$ as the device operates from the triode to saturation mode in the absence of hot carrier effects. The diffusion noise simulation results are plotted in Figure 1-13. As expected the diffusion noise is lowered to $2/3$ of the value recorded at low V_{ds}, as the drain bias increases beyond $V_{gs} - V_t$. With $V_t = 0.932$ V, noise spectral density contributions at the drain contact for electrons and holes are plotted in Figures 1-14a and 1-14b, respectively. In the triode mode of operation, the noise due to electrons dominates. The channel is the critical region for producing the overall diffusion noise observed at the drain terminal, as the simulation shows in Figure 1-14a.

1.3 Organization and Overview

This dissertation is divided into five chapters, including this introduction. Chapter 2 provides the theory behind the bulk g-r noise. Two different implementation methods are described in detail. The "direct" method places the added trap electron continuity equation directly into the system. Noise sources in each equation are coupled out to the external contact through its Green's function. The "indirect" method implements the effect of the added trap level through back substitution. Thus the noise sources in the added trap continuity equation are back-substituted to the Poisson, electron, and hole continuity equations before they are coupled out to the external contact through the modified scalar Green's functions. Both methods are compared, and their simulation results are presented at the end of the chapter.

From the simulation results shown in Chapter 2, the bulk g-r noise in active CMOS and bipolar devices is eliminated as the possible cause of the $1/f$ noise observed at low frequencies. The focus is then moved to the Si/SiO$_2$ interface region. Although the theory behind the g-r noise at the interface is very similar to the theory in the bulk, the differences between these two cases must be considered. Chapter 3 discusses how the distributed trap energy at the interface is taken into consideration by the simulator. In addition, the conversion from a 3D bulk g-r simulation to a 2D interface g-r simulation is also described in detail. The chapter ends with the interface noise simulation results.

The simulation results in Chapter 3 also point out that the interface trap noise is not the source of low-frequency $1/f$ noise. Thus the focus of the research is pointed to the noise produced by the defects in the oxide. Chapter 4 provides the theory behind the oxide trapping noise, which is caused by the trapping and detrapping of carriers from the channel to the traps in the oxide via trap centers at the interface. The "Capture and Tunneling" model describes how carriers first get trapped by the fast defect centers at the interface, and then tunnel to the trap centers in the oxide at equal energy level. Depending on the spatial position of the oxide trap from the interface, the characteristic time that determines the length of a carrier staying in the trap centers is distributed. Distributions of different characteristic times from different trap locations can then be transformed to the frequency domain. Thus the Lorentzian spectra from these sources have their corner frequencies evenly distributed, in the case of a homogeneous trap distribution, to produce $1/f$-like noise at low frequencies. Two critical factors that govern the outcome of the oxide trapping noise are the oxide defect density distribution and the carrier tunneling rate. Both factors affect the magnitude and the slope of the $1/f$ simulated noise results. The modeling of the defect density distribution in energy and in the spatial domain is discussed in detail, so is the shape of energy barrier for tunneling carriers.

Generation-recombination noise associated with bulk defect levels is modeled in a partial differential equation-based device simulator using the impedance field method to determine the maximum allowable defect density that guaranties generation-recombination noise-free operation at all bias conditions. In Chapter 5, a detailed comparison of simulated and analytical noise data shows that this density can be estimated accurately even in the presence of hot carrier effects and space charge injection. In addition the noise simulations reveal that the g-r noise plateau value reaches a maximum as a function of bias and then decreases at higher bias due to space charge injection and carrier heating which reduce the local strength and the transfer function of the distributed noise sources, respectively.

Chapter 6 consists of conclusions and suggestions for future research.

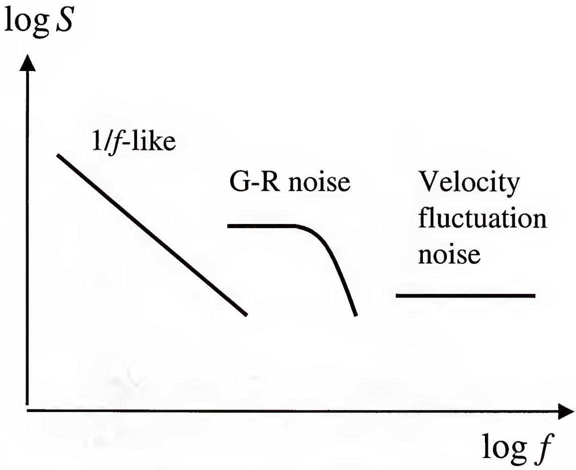

Figure 1-1. Different types of noise observed in a noise experiment

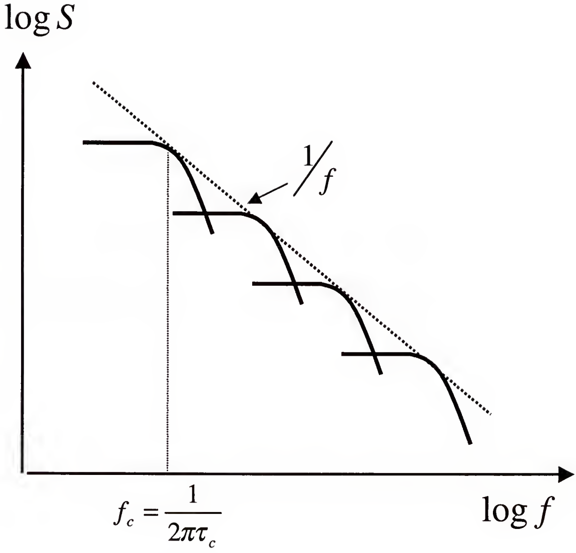

Figure 1-2. Low-frequency 1/f-like noise produced from a superposition of Lorentzian spectra, caused by the g-r mechanism

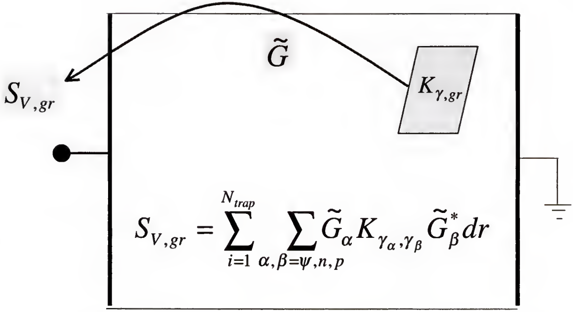
$\tilde{G}$
$S_{V,gr}$
$K_{\gamma,gr}$
$S_{V,gr} = \sum_{i=1}^{N_{trap}} \sum_{\alpha,\beta=\psi,n,p} \tilde{G}_\alpha K_{\gamma_\alpha,\gamma_\beta} \tilde{G}_\beta^* dr$

Figure 1-3. Local g-r noise strength to the external contact through the scalar Green's function

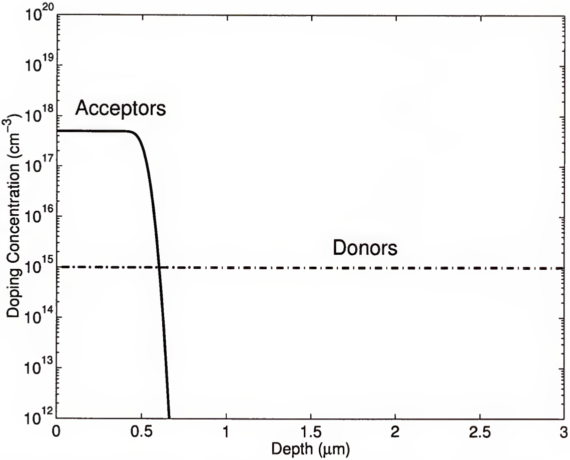

Figure 1-4. Doping profile of a pn diode. The emitter region with a peak acceptor concentration of $5 \cdot 10^{17}$ cm^{-3} is implanted in a uniformly doped base substrate with a 10^{15} cm^{-3} donor concentration.

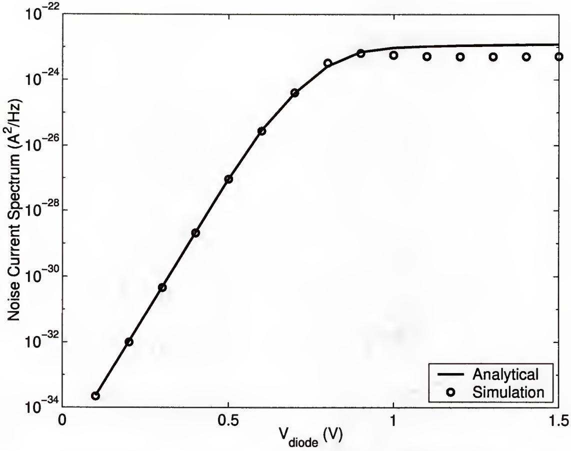

Figure 1-5. Current noise spectral density vs. diode voltage. The analytical and simulation results are compared. Note that the analytical result is only valid under low injection conditions.

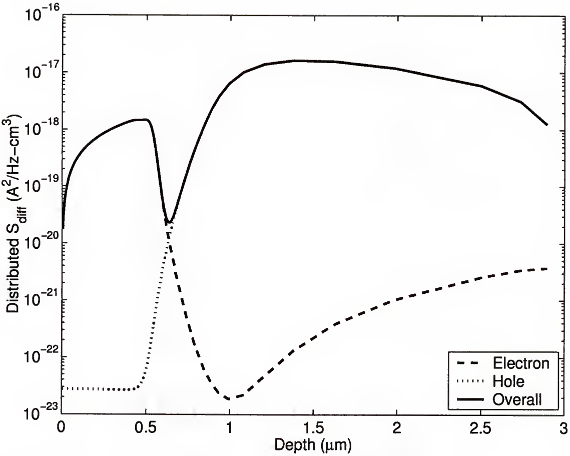

Figure 1-6. Distributed current noise spectral density for both carriers, under low injection conditions (V_{diode} = 0.4 V)

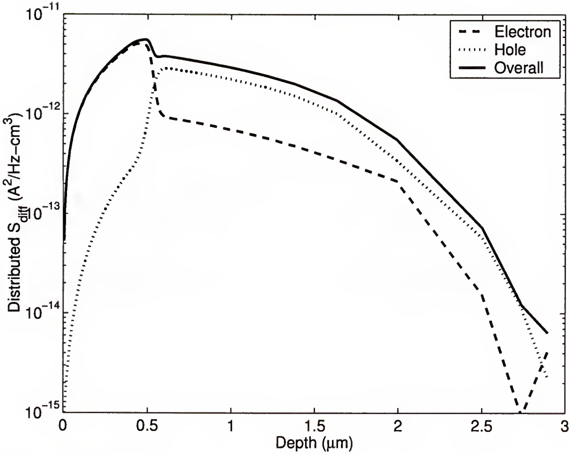

Figure 1-7. Distributed current noise spectral density for both carriers, under high injection conditions (V_{diode} = 1.4 V)

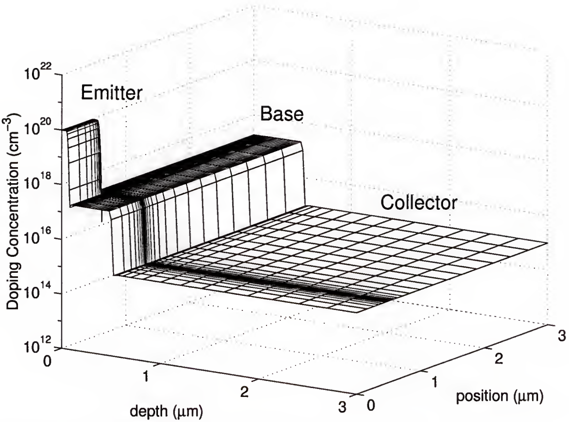

Figure 1-8. Doping profile of a npn BJT structure

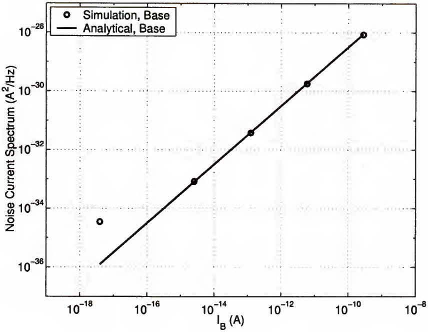

(a)

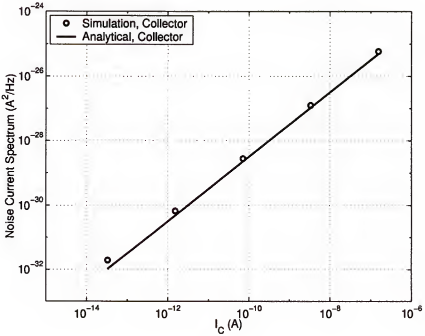

(b)

Figure 1-9. Current noise spectral density vs. bias current. The collector is biased at 1.0 V, while the base is swept from 0.3 to 0.7 V. (a) Noise at the base terminal. (b) Noise at the collector terminal.

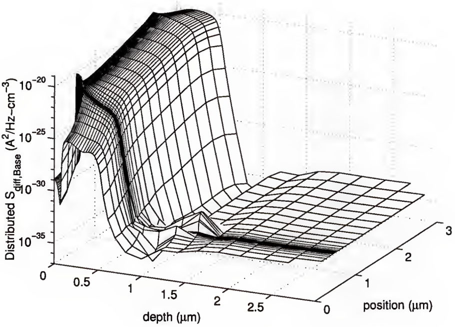

(a)

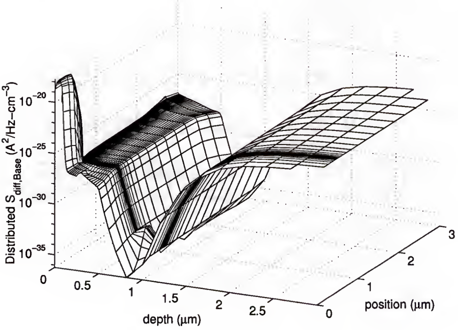

(b)

Figure 1-10. Distributed current noise spectral density at the base contact under low injection condition (V_{ce} = 1.0 V, V_{be} = 0.5 V). (a) Electron component. (b) Hole component.

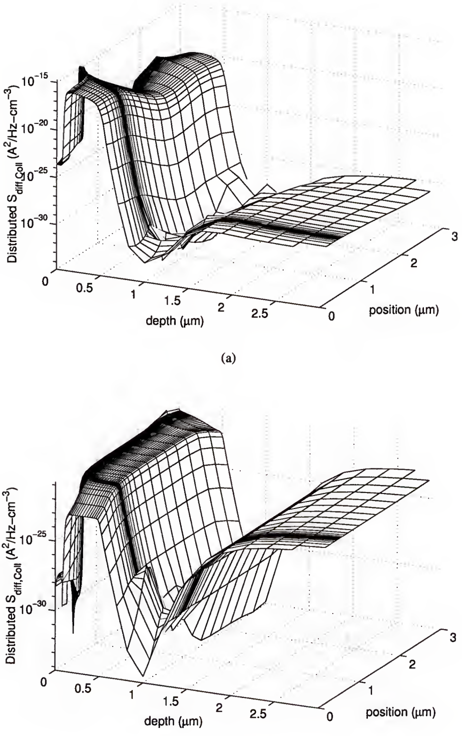

(a)

(b)

Figure 1-11. Distributed current noise spectral density at the collector contact under low injection condition (V_{ce} = 1.0 V, V_{be} = 0.5 V). (a) Electron component. (b) Hole component.

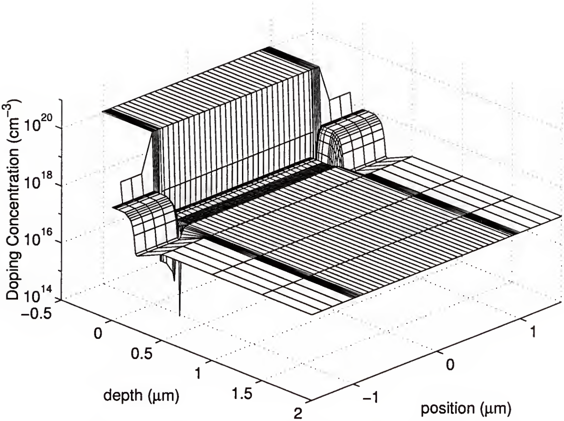

Figure 1-12. Doping profile of a n-channel MOSFET. The channel length is about 2 μm.

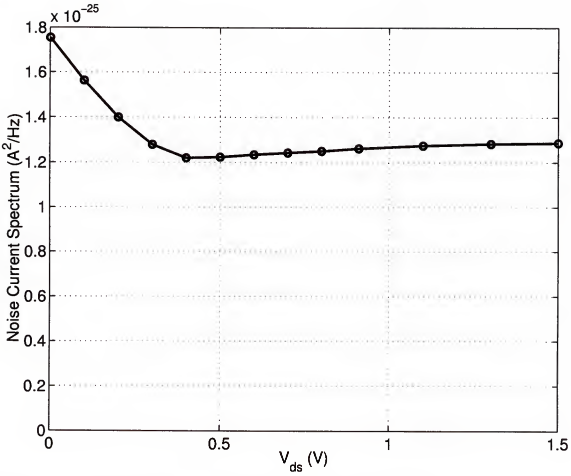

Figure 1-13. Current noise spectral density vs. drain bias voltage (V_{gs} = 1.5 V)

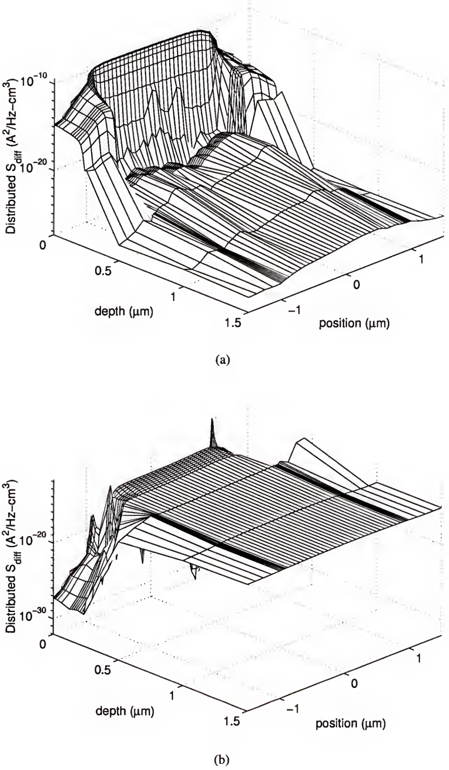

Figure 1-14. Distributed current noise spectral density contributions at the drain contact (V_{ds} = 1.5 V, V_{gs} = 0.4 V). (a) Electron component. (b) Hole component.

CHAPTER 2
BULK GENERATION-RECOMBINATION NOISE

2.1 Introduction

Many defects that exist in semiconductor devices are usually unintentional. Elements such as Carbon, Oxygen, and various metals are introduced to the wafer during process steps, and then become carrier trap centers that affect device performance and produce generation-recombination (g-r) noise. This g-r noise is due to the fluctuation of the number of carriers in the conduction and valence bands. Carriers get trapped and de-trapped from the defect trap centers in the forbidden band gap, causing the number of carriers in the continuum states to fluctuate. This in turn causes the current or the voltage, depending on the condition at the contact terminal, to fluctuate as well. This type of carrier transition has generally been characterized by the Shockley-Read-Hall model. In this model, each defect center is specified by its defect density, its carrier capture coefficients, and its energy position relative to either the conductance or valence band. Due to the possible varieties of defects present in the device, there might be one dominant defect center, or multiple defect centers across the entire active region. In addition, defects are distributed over space as they are more likely to accumulate at or near the surface or the metallurgical junctions.

As mentioned previously, there are different factors that would affect the outcome of the g-r noise. For example, device-operating temperature governs the Fermi level, which sets the trap occupancy factor that limits the probability of carrier transitions. The carrier transition rate increases as the Fermi level approaches the trap energy position. When the Fermi level lines up with the trap energy position, the traps are half filled, allowing maximum probability of the carriers to get trapped and de-trapped from the defect centers. Since the Fermi level is a function of the carrier concentration, the doping concentration is another factor to determine which trap states are critical for generating the g-r noise. Another factor that governs the g-r noise is the bias across the device. Both the local noise strength and the Green's function, which transfers the fluctuation at each differential volume of the device to a specific contact, change with the bias. Thus we also expect the magnitude of the g-r noise to change with the bias. For example, the simple analytical derivation of the g-r noise of a bulk resistor will show that the current noise spectral density is proportional to I^2 or E^2, where I is the current and E is the field across the device.

2.2 Theory

As mentioned previously, the g-r process can best be described by the Shockley-Read-Hall model, as shown in Figure 2-1. For illustration purpose, assume there is one defect trap center in the bandgap, and the traps are acceptor-like. In addition to the three basic equations

$$F_\psi = -\frac{d^2\psi}{dr^2} - \frac{q}{\varepsilon}\left[p - n + N_D^+ - N_A^- - n_t\right] = 0 \tag{2.1}$$

$$F_n = \frac{dn}{dt} - \frac{1}{q}\nabla \cdot J_n - g_n + r_n - \gamma_n(r,t) = 0 \tag{2.2}$$

$$F_p = \frac{dp}{dt} + \frac{1}{q}\nabla \cdot J_p - g_p + r_p + \gamma_p(r,t) = 0 \tag{2.3}$$

a trapped electron continuity equation is added to describe the carrier transition at the trap level [11]

$$F_{n_t} = \frac{dn_t}{dt} + g_n - r_n - g_p + r_p - \gamma_t(r,t) = 0 \tag{2.4}$$

where γ_n, γ_p, and γ_t are the Langevin noise terms describing transition rate fluctuations. The transition rates can be expressed as

$$r_n = c_n n (N_T - n_t) \tag{2.5}$$

$$g_n = c_n n_1 n_t \tag{2.6}$$

$$r_p = c_p p n_t \tag{2.7}$$

$$g_p = c_p p_1 \left(N_T - n_t\right) \tag{2.8}$$

where n_1 and p_1 are the Shockley parameters

$$n_1 = N_C \Im_{1/2}\left(\frac{E_t - E_C}{kT}\right) \approx N_C \exp\left(\frac{E_t - E_C}{kT}\right) \tag{2.9}$$

$$p_1 = N_V \Im_{1/2}\left(\frac{E_V - E_t}{kT}\right) \approx N_V \exp\left(\frac{E_V - E_t}{kT}\right) \tag{2.10}$$

with the assumption that the trap level is at least a few kT from the conductance and valence bands. In these equations the defect species are specified by three parameters: trap energy level (E_T), trap density (N_T), and capture coefficients (c_n, c_p).

Two approaches can be taken to solve for ψ, n, p, and n_t. One approach, called the "direct" approach, is to place the four listed equations into FLOODS and solve for the four variables simultaneously. The other approach, called the "indirect" approach, is to eliminate the added trap electron continuity equation by mapping the trapped electron density n_t and the noise term γ_t from Equation (2.4) into Equation (2.1), (2.2), and (2.3). Choosing the best method to implement depends on how the simulator formulates the PDEs to the system.

In the previous versions of FLOODS, each PDE was hard coded into the system using C++ scripts. Since hard-coding extra equations into the system is difficult to implement, it is easier to just modify the pre-existing components of the Jacobian matrix for the three basic equations of the drift-diffusion model. In this case, the second approach is preferred. Each trap electron continuity equation is back substituted to the original three equations through modifications of the matrix components. The advantage of this approach is that no additional data storage is needed and little programming overhead is involved, since the three basic equations for the calculation of ψ, n, p are already implemented in FLOODS. In addition, since there are only three equations and three variables to solve, a faster convergence can be achieved in simulation.

The current version of FLOODS was rewritten to accept scripting of PDEs. The user can now add or delete equations in the system on demand by describing the equations in the command scripts. In this case, the direct approach is preferred, since adding the extra trap continuity equation to account for the added trap level can easily be specified. The programming overhead for adding equations to the system is not an issue anymore. Although the benefits which come from the indirect approach disappear in this method, the noise contributions from different trap levels can now be displayed and separated individually. Both methods of implementation are discussed in detail below.

2.3 "Indirect" Approach

The full ac noise matrix equation is defined as $[\tilde{J}][\tilde{x}] = [\tilde{b}]$ where $[\tilde{J}]$ is the small-signal, frequency domain, Jacobian matrix defined as

$$[\tilde{J}] = \begin{bmatrix} \frac{dF_\psi}{d\psi} & \frac{dF_\psi}{dn} & \frac{dF_\psi}{dp} & \frac{dF_\psi}{dn_t} \\ \frac{dF_n}{d\psi} & \frac{dF_n}{dn} + j\omega & \frac{dF_n}{dp} & \frac{dF_n}{dn_t} \\ \frac{dF_p}{d\psi} & \frac{dF_p}{dn} & \frac{dF_p}{dp} + j\omega & \frac{dF_p}{dn_t} \\ \frac{dF_{n_t}}{d\psi} & \frac{dF_{n_t}}{dn} & \frac{dF_{n_t}}{dp} & \frac{dF_{n_t}}{dn_t} + j\omega \end{bmatrix} \tag{2.11}$$

with

$$[\tilde{x}] = \begin{bmatrix} \tilde{\psi} \\ \tilde{n} \\ \tilde{p} \\ \tilde{n}_t \end{bmatrix} \quad [\tilde{b}] = \begin{bmatrix} 0 \\ \tilde{\gamma}_n \\ \tilde{\gamma}_p \\ \tilde{\gamma}_{n_t} \end{bmatrix} \tag{2.12}$$

Knowing the terms $\frac{dF_\psi}{dn_t}$, $\frac{dF_n}{dn_t}$, $\frac{dF_p}{dn_t}$, $\frac{dF_{n_t}}{d\psi}$, $\frac{dF_{n_t}}{dn}$, $\frac{dF_{n_t}}{dp}$, and $\frac{dF_{n_t}}{dn_t}$ allows $\tilde{n}_t$ to be back-substituted into the first three equations to get

$$\begin{bmatrix} \frac{dF'_\psi}{d\psi} & \frac{dF'_\psi}{dn} & \frac{dF'_\psi}{dp} \\ \frac{dF'_n}{d\psi} & \frac{dF'_n}{dn}+j\omega & \frac{dF'_n}{dp} \\ \frac{dF'_p}{d\psi} & \frac{dF'_p}{dn} & \frac{dF'_p}{dp}+j\omega \end{bmatrix} \begin{bmatrix} \tilde{\psi} \\ \tilde{n} \\ \tilde{p} \end{bmatrix} = \begin{bmatrix} \tilde{B}_\psi \\ \tilde{B}_n \\ \tilde{B}_p \end{bmatrix} \tag{2.13}$$

where $\tilde{B}_\psi$, $\tilde{B}_n$, and $\tilde{B}_p$ are the noise terms in the modified Poisson's, electron, and hole continuity equations, respectively. These terms are functions of γ_t, γ_n, and γ_p, and equal to

$$\tilde{B}_\psi = \left(\frac{q}{\varepsilon_s\varepsilon_o}\right)\frac{\tau_t}{1+j\omega\tau_t}\tilde{\gamma}_t \tag{2.14}$$

$$\tilde{B}_n = \tilde{\gamma}_n + \frac{c_n\left(n+n_1\right)\tau_t}{1+j\omega\tau_t}\tilde{\gamma}_t \tag{2.15}$$

$$\tilde{B}_p = -\tilde{\gamma}_p - \frac{c_p\left(p+p_1\right)\tau_t}{1+j\omega\tau_t}\tilde{\gamma}_t \tag{2.16}$$

where the trap time constant is defined as

$$\tau_t = \left[c_n\left(n+n_1\right)+c_p\left(p+p_1\right)\right]^{-1} \tag{2.17}$$

c_n and c_p are the electron and hole capture coefficients, and n_1 and p_1 are the Shockley parameters. The strength of the modified noise sources for GR become

$$K_{\gamma'_t,\gamma'_t} = \left(\frac{q}{\varepsilon_s\varepsilon_o}\right)^2\frac{\tau_t^2}{1+\omega^2\tau_t^2}K_{\gamma_t,\gamma_t} \tag{2.18}$$

$$K_{\gamma'_n,\gamma'_n} = K_{\gamma_n,\gamma_n} - 2X_nK_{\gamma_n,\gamma_t} + \left(X_n^2+Y_n^2\right)K_{\gamma_t,\gamma_t} \tag{2.19}$$

$$K_{\gamma'_p,\gamma'_p} = K_{\gamma_p,\gamma_p} - 2X_pK_{\gamma_p,\gamma_t} + \left(X_p^2+Y_p^2\right)K_{\gamma_t,\gamma_t} \tag{2.20}$$

plus the other less important cross-correlated terms. The variables X_n and X_p are defined by

$$X_n = \frac{-c_n(n+n_1)\tau_t}{1+\omega^2\tau_t^2} \quad Y_n = -\omega\tau_t X_n \tag{2.21}$$

$$X_p = \frac{c_p(p+p_1)\tau_t}{1+\omega^2\tau_t^2} \quad Y_p = -\omega\tau_t X_p \tag{2.22}$$

The g-r noise source strengths defined in [11] are

$$K_{\gamma_n,\gamma_n} = 2g_n + 2r_n = -K_{\gamma_n,\gamma_t} \tag{2.23}$$

$$K_{\gamma_p,\gamma_p} = 2g_p + 2r_p = -K_{\gamma_p,\gamma_t} \tag{2.24}$$

$$K_{\gamma_t,\gamma_t} = K_{\gamma_n,\gamma_n} + K_{\gamma_p,\gamma_p} \tag{2.25}$$

Implementation of the equations above into FLOODS enables the program to calculate the g-r noise voltage spectral density at an external contact from

$$S_{V,gr} = \sum_{i=1}^{Ntrap} \sum_{\alpha,\beta=\psi,n,p} \int_{vol} \tilde{G}_\alpha K_{\gamma_\alpha,\gamma_\beta} \tilde{G}_\beta^* dr \tag{2.26}$$

where N_{trap} is the number of trap levels in the device and $\tilde{G}$ is the Green's function modified to account for the correlation between trap transition rates.

As mentioned previously, to reduce the overhead of adding the trapped electron continuity equation as the forth equation to the system, the dc value of n_t can be analytically calculated and back substituted into the first three equations. Under dc condition, $g_n - r_n = g_p - r_p$. The dc value of n_t can be obtained from this equality:

$$n_t = \frac{(c_n n + c_p p_1) N_T}{c_n(n+n_1) + c_p(p+p_1)} \tag{2.27}$$

By substituting this into Poisson's, electron, and hole continuity equations, the changes in the device dc characteristics due to the effect of traps are accounted for.

A similar approach has also been explored by Bonani [5] independently, showing again that the Langevin noise terms associated with trap-assisted transitions specified in the trap electron continuity equation are back-substituted to the Poisson, electron, and hole continuity equations. Thus the modified Langevin noise terms exist in all three PDEs. The local noise source strengths from his derivation are equivalent to the ones in Equations (2.18)-(2.20) above.

2.4 "Direct" Approach

As mentioned previously, the full ac noise matrix equation is defined as $[\tilde{J}][\tilde{x}] = [\tilde{b}]$. Since there is no back substitution to eliminate any equation, the Jacobian matrix $[\tilde{J}]$ in Equation (2.11) is the exact matrix implemented in the system. The matrix $[\tilde{x}]$ and $[\tilde{b}]$ implemented in the system are also the same as the one specified in Equation (2.12). The g-r noise strengths are defined in Equation (2.23) through (2.25). The g-r noise voltage spectral density can then be calculated from

$$S_{V,gr} = \sum_{i=1}^{Ntrap} \sum_{\alpha,\beta=\psi,n,p,n_t} \int_{vol} \tilde{G}_\alpha K_{\gamma_\alpha,\gamma_\beta} \tilde{G}^*_\beta dr \tag{2.28}$$

where N_{trap} and $\tilde{G}$ are the number of trap levels and the scalar Green's function, respectively.

2.5 Simulation Verification

Extensive research on bulk g-r noise has been done by Van Vliet and Van der Ziel, for either single or multiple defect trap systems. As stated in their published work [11, 12], the derivation of the noise spectrum starts with the fluctuation in the trap electron continuity equation

$$\frac{d\Delta n_t}{dt} = -\frac{\Delta n_t}{\tau_t} + \gamma_t \tag{2.29}$$

where the trap time constant τ_t is defined as

$$\tau_t = [c_n(n+n_1) + c_p(p+p_1)]^{-1} \tag{2.30}$$

Taking the Fourier transform of Equation (2.29), the fluctuation spectrum for the number of trapped carriers in a small differential volume Δv equals

$$S_{\Delta n_t,\Delta v}(f) = \frac{S_{\gamma_t}\tau_t^2}{1+\omega^2\tau_t^2} \tag{2.31}$$

where $\omega = 2\pi f$. From the Poisson/Gaussian law, the spectrum of γ_t is equal to

$$S_{\gamma_t} = \lim_{\tau\to\infty} 2\tau\overline{\gamma_t\gamma_t^*} = \frac{2}{\tau}\overline{\Delta n_t} = 2\left(g_n + r_n + g_p + r_p\right)/\Delta v \tag{2.32}$$

Equation (2.31) becomes

$$S_{\Delta n_t,\Delta V}(f) = \frac{2\left(g_n + r_n + g_p + r_p\right)\tau_t^2}{\left(1+\omega^2\tau_t^2\right)\Delta v} \tag{2.33}$$

where the value at low frequency plateau is

$$S_{\Delta n_t,\Delta V}(f\to 0) = 2\left(g_n + r_n + g_p + r_p\right)\tau_t^2 \tag{2.34}$$

To verify this expression, a 2-D n$^+$-n-n$^+$ bulk resistor is created. The n- and n$^+$-region are doped with N_d = 10^{15} and N_{d+} = 10^{18} cm^{-3} donor ions, respectively. The length of the n-region L is 2 μm, and the n$^+$-regions are 0.5 μm long on each side. Its cross-section area A is 1 μm^2. A defect center E_T, 0.3 eV below the conduction band E_C, is specified in the simulation. Its capture coefficients, c_n and c_p, and defect density N_T are set to 10^{-8} cm^3/s and 10^{12} cm^{-3}, respectively. Since E_T is much closer to E_C than E_V, one can safely assume $g_n, r_n >> g_p, r_p$ and $g_n \approx r_n$. Equation (17) above is then simplified to

$$S_{\Delta n_t,\Delta V} = \frac{4r_n\tau_t^2}{\left(1+\omega^2\tau_t^2\right)\Delta v} = \frac{4g_n\tau_t^2}{\left(1+\omega^2\tau_t^2\right)\Delta v} \tag{2.35}$$

Constrained by the law of space charge neutrality, the fluctuation in the number of trap carriers at the trap level is equal to the fluctuation of carriers in the continuum states. Thus,

$$S_{\Delta n_t} = S_N \tag{2.36}$$

where N is the total number of carriers in the conduction band. For number fluctuations such as the bulk g-r noise in an ohmic device, the noise spectral density relation is

$$\frac{S_N}{N^2} = \frac{S_V}{V^2} = \frac{S_I}{I^2} \tag{2.37}$$

where V and I are the dc biases of the device. Substituting Δv with LA, the entire volume of the n-region, and N with LAN_d, the current spectral density of the resistor now equals

$$S_I(f) = \frac{I^2}{N^2} S_N(f) = \frac{4I^2 g_n \tau_t^2}{LAn^2} \cdot \frac{1}{1+\omega^2\tau_t^2} \tag{2.38}$$

Since $c_n(n+n_1) >> c_p(p+p_1)$, τ_t can be simplified as $\tau_t \approx [c_n(n+n_1)]^{-1}$. The analytical expression of the current noise spectral density of this structure at low frequencies becomes

$$S_I(f \to 0) \approx \frac{4I^2}{LAn^2} \frac{n_1 n_t}{c_n(n+n_1)^2} \tag{2.39}$$

where $n \approx N_d$. For verification the calculated value of this equation is used against the simulation data.

The g-r noise for the n$^+$-n-n$^+$ bulk resistor with the defect trap center described above is simulated. The current noise spectral density from the simulation is plotted against the analytical g-r noise expression (2.38), shown in Figure 2-2. The simulated noise is in good agreement with the theory. The simulated bulk g-r noise rolls off at the calculated corner frequency $f_c = 1/2\pi\tau_t \approx 2$ MHz, and has a slope of $1/f^2$ beyond f_c. These results are indeed able to prove the validity of the bulk g-r noise simulation package in FLOODS. Simulations results from sweeping the trap energy level through the upper half of the energy band gap are plotted in Figure 2-3. As expected the noise spectral density calculated at $f = 1$ Hz reaches a maximum when the trap energy level is at or near the Fermi level. When the Fermi level equals the trap energy level, the trap is half-occupied by the carriers. This condition meets the highest carrier transition probability, thus in turn maximizes the g-r noise. As for this device with N_d = 10^{15} cm^{-3}, the Fermi level is calculated to be 0.265 eV below the conduction band.

The g-r noise simulations on an old version of FLOODS with the "indirect" approach were compared with the simulations on the current version of FLOODS with the "direct" approach. The simulation results came out the same as expected.

Measurements on a multi-trap p^+-p-p^+ silicon resistor [13] are also used to validate the noise simulation. The voltage noise spectral density and the characteristic time τ_t of each g-r trap state are simulated as a function of temperature. The purpose for varying the temperature was to shift the Fermi level, as shown in Figure 2-4. As the Fermi level crosses a trap state, the low frequency g-r noise plateau value due to that trap will reach a maximum, as shown in Figure 2-5. In this figure, the open circles and the solid curves represent the measured and simulated data, respectively. This representation will be used for the subsequent figures, unless specified otherwise. The four maxima suggest there are four trap states that are electrically active. By varying the energy position of each trap state and matching the noise simulation results with the measured data, the energy position of each trap can be found. By adjusting the trap density, the magnitude of the simulated noise level can be matched to the measurement data. At each temperature, the characteristic time τ_t of each g-r trap was determined. The results are shown in Figure 2-6. By adjusting the values of the hole capture coefficients, the simulation could match the measured data. Since the noise spectral density of each g-r trap is affected by its energy level position, hole capture coefficient c_p, and trap concentration N_T, the FLOODS simulations and procedures of adjusting these parameters need to be done iteratively. The results are shown in Table 2-1.

G-R noise simulations were carried out on the same NMOS structure that was used in the example for the diffusion noise in Chapter 1, of which the channel length is 2 μm. In the first test with this structure, three defect trap centers are specified in the bulk, one located at E_i (specified to be Acceptor-like), one 0.3 eV below E_C (specified to be Donor-like), and the other one 0.3 eV above E_V (specified to be Acceptor-like). Allowing defect densities to be uniformly distributed and equal to $N_T = 10^{10}$ cm^{-3}, and the capture coefficients $c_n = c_p = 10^{-7}$ cm^3/s to be the same for all three traps, the gate bias of this device is first driven to 1.5 V. For this device the threshold voltage extracted from the dc simulations is equal to 0.932 V. Noise simulation results at 1 Hz are plotted in Figure 2-7 with the drain to source voltage V_{ds} sweeping from the triode to the saturation mode of operation. From these results, we found the traps with the parameters specified above cannot produce an overall g-r noise higher than the background diffusion noise. Another observation is that the defect centers at or near E_i are most effective on producing the bulk g-r noise in this MOSFET structure. This suggests the bulk g-r traps in the space charge region play an important role, since this region is where the Fermi level crosses the energy levels of those defect centers. Taking a closer look of where the noise is generated, the distributed current noise spectral density of the bulk g-r noise for the device operating in the linear mode is plotted in Figure 2-8. We found that in addition to the noise produced from the space charge region due to the reason described above, the majority of the bulk g-r noise contribution is stemming from the channel of the device, due to the vast amount of the carriers in that region.

Since the first test has shown that the bulk g-r noise is mostly coming from the trap centers at or near E_i, in the second test only the trap at E_i is considered. The defect density is again set to $N_T = 10^{10}$ cm^{-3}. This time the capture coefficients are swept from 10^{-6} to 10^{-8} cm^3/s. The results are shown in Figure 2-9. They illustrate that the bulk g-r noise increases as the capture coefficient decreases. In addition, it has the potential to become higher than the diffusion noise. To investigate this further, noise as a function of frequency is simulated. The result is plotted in Figure 2-10. As this figure shows, changing the capture coefficient does not just change the low frequency noise magnitude, but it also changes the corner frequency. Even though the bulk g-r noise from the trap centers with the capture coefficient of 10^{-8} cm^3/s manages to become higher than the diffusion noise, its effect is not significant to produce a g-r bump on 1/f-like noise that has a corner frequency in the MHz range. The final test focuses again on the defect centers at E_i. With the capture coefficients set to 10^{-7} cm^3/s, the defect density N_T is swept from 10^9 to 10^{11} cm^{-3}. The result is plotted in Figure 2-11. As expected, a higher defect density produces higher bulk g-r noise.

These simulations have demonstrated that the g-r bulk mechanism in MOS structures is not the dominant noise source at low frequencies. With reasonable parameters, it is hardly able to overshadow the diffusion noise. For the traps that produce noise higher than the diffusion noise, their noise spectrum is usually not high enough to surpass the $1/f$-like noise that dominates at low frequencies. Yet the Lorentzian produced by the bulk g-r noise might be one of the candidates that produces the Random Telegraph Signal noise that has been seen in ultra short-channel devices.

Table 2-1. Information on each G-R trap

	Energy position (eV)	Hole capture coefficient (cm^3s^{-1})	Concentration (cm^{-3})
T1	$E_v + 0.405$	$6.0 \cdot 10^{-9}$	$2.0 \cdot 10^{11}$
T2	$E_v + 0.300$	$4.0 \cdot 10^{-9}$	$1.1 \cdot 10^{12}$
T3	$E_v + 0.155$	$9.0 \cdot 10^{-10}$	$2.0 \cdot 10^{10}$
T4	$E_v + 0.120$	$2.5 \cdot 10^{-10}$	$1.0 \cdot 10^{9}$

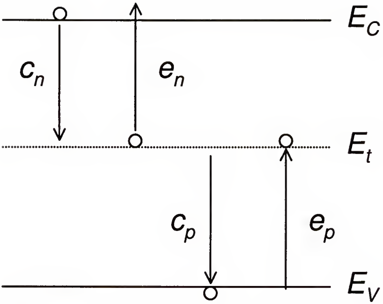

Figure 2-1. Carrier transitions between the continuum states and localized defect states

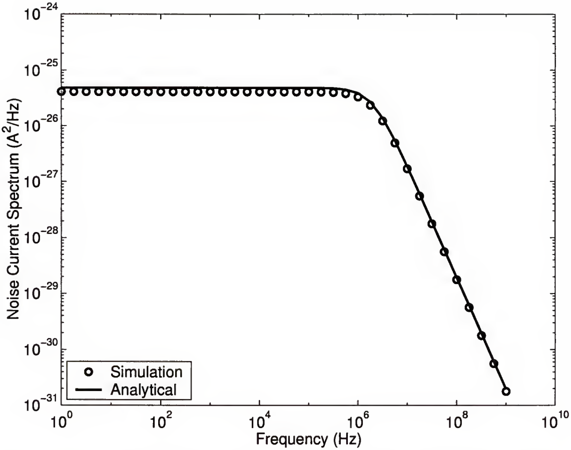

Figure 2-2. Comparison between the simulated and analytical current noise spectral density as a function of frequency. The bias across the device is set to 0.1 V.

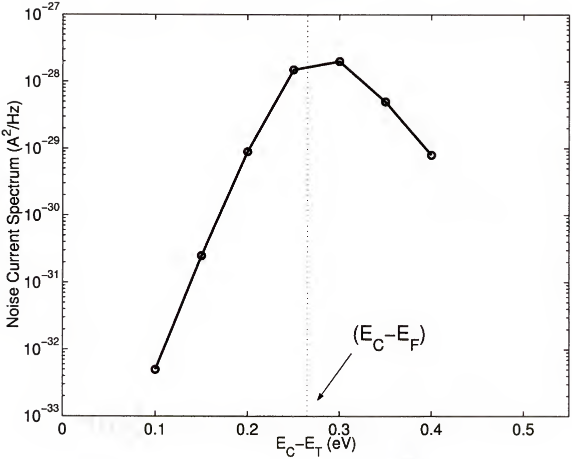

Figure 2-3. Bulk g-r noise simulated as a function of trap energy level (*f* = 1 Hz)

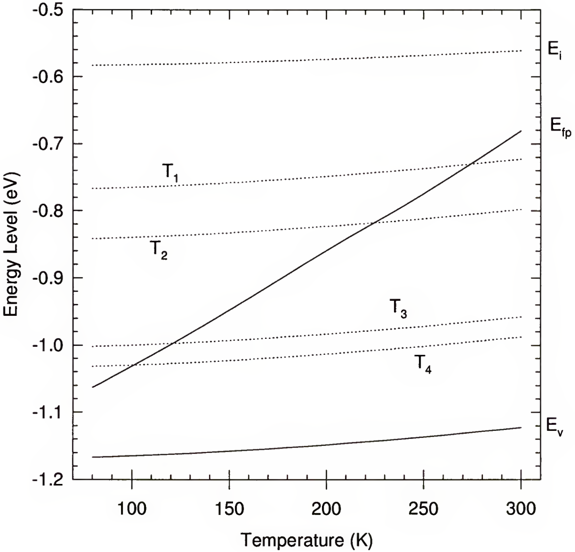

Figure 2-4. Fermi and g-r trap energy levels. The energy levels of g-r traps are represented by the dashed lines, and the position of the Fermi level is shown by the solid line.

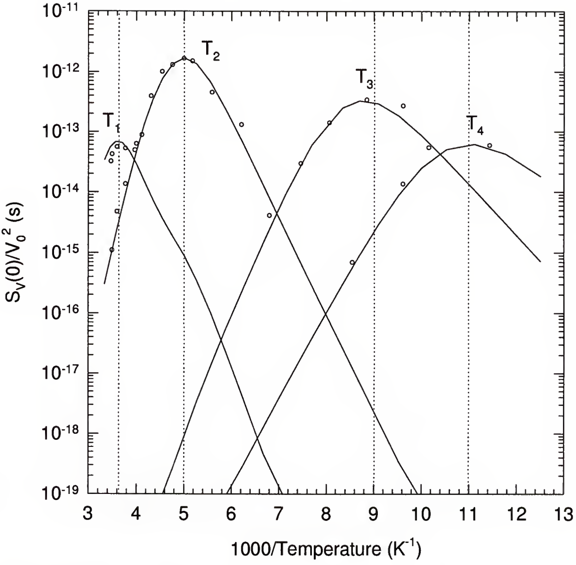

Figure 2-5. Low frequency g-r noise plateau $S_v(0)/V_o^2$ versus $1000/T$

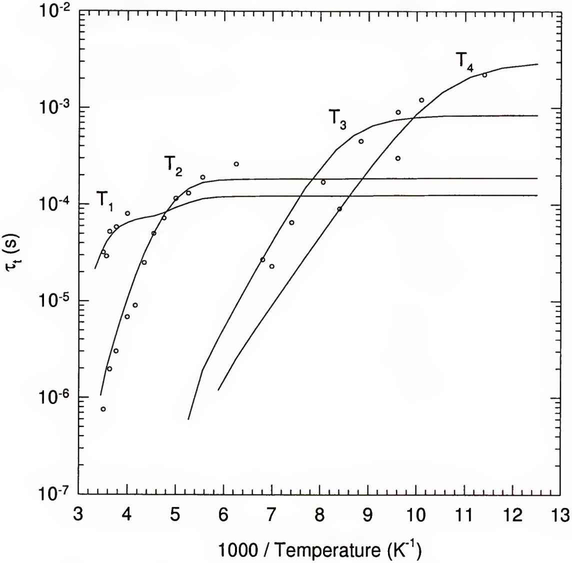

Figure 2-6. Characteristic time τ_t of different traps versus $1000/T$

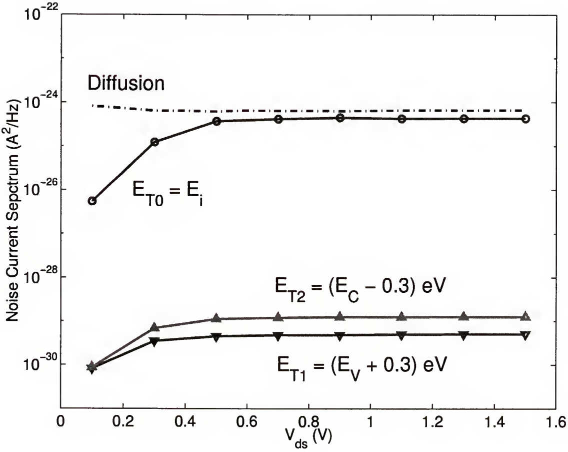

Figure 2-7. Noise from different bulk g-r trap centers

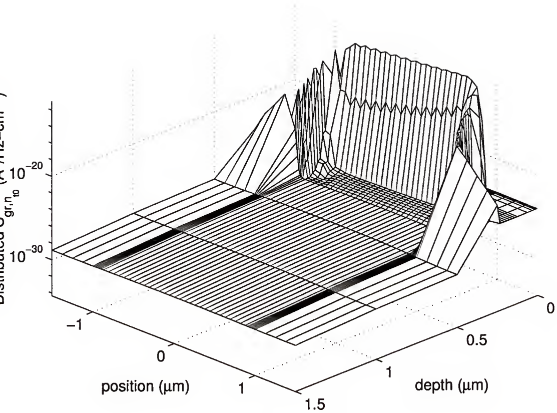

Figure 2-8. Distributed current noise spectral density (f = 1 Hz) of the MOS structure operating in the triode mode of operation (V_{gs} = 1.5 V, V_{ds} = 0.3 V, and V_t = 0.932 V)

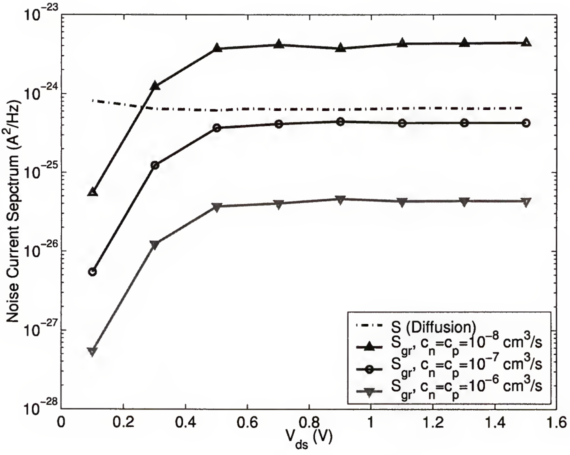

Figure 2-9. Noise simulated with different capture coefficients

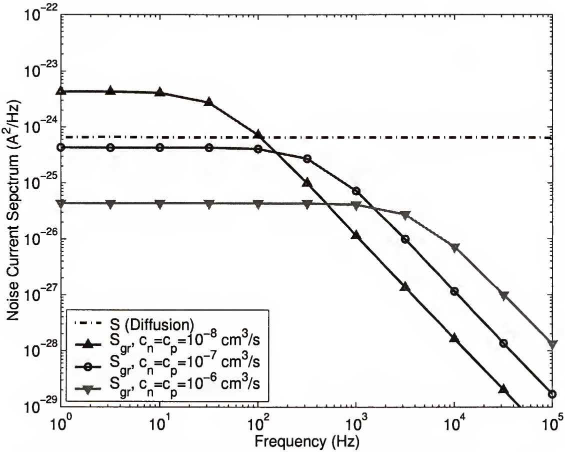

Figure 2-10. Noise with different capture coefficients plotted as a function of frequency

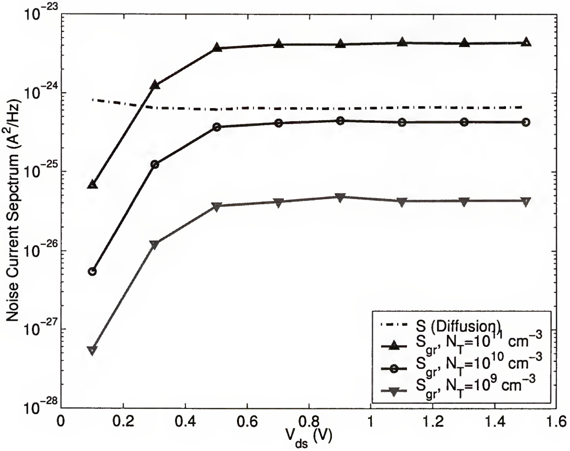

Figure 2-11. Noise simulated with different defect densities

CHAPTER 3
INTERFACE GENERATION-RECOMBINATION NOISE

3.1 Introduction

The number of defects at a device interface is generally considered to be large when compared with the defects in the bulk or in the oxide. This is due to the termination of periodic structures and lattice mismatch. In some cases, the defects are also due to the presence of oxygen and other impurities. These defects can become the generation-recombination (g-r) centers for the carriers at the surface. Sometimes they also become the stepping-stone for the carriers to tunnel into the defects in the oxide. For MOS devices, surface g-r noise mechanisms like interface trapping noise and oxide trapping noise have strong effects on the devices overall noise performance, since carriers are moving toward the surface to form a channel. In this chapter, the interface g-r noise mechanism will be discussed in detail.

3.2 Theory

Unlike the defect traps in the bulk that are discrete in nature, the defect traps at the interface and in the oxide are distributed in energy over the bandgap, due to the variety of defects available at the interface. A few techniques can be used to measure the trap density distributions at the interface. Among them are Deep-Level Transient Spectroscopy (DLTS) and the conductance method [14]. Although the DLTS can obtain good results for the traps near the mid-gap region, it is less suitable for traps near the band edges. In comparison, the conductance method gives more accurate and reliable results for the traps distributed over the bandgap. An example of measurement results is shown in Figure 3-1 [14]. In the past, this trap density distribution was modeled by an exponential function

$$N_t(E) = N_0 \exp\left[\xi \left|E - E_i\right|\right] \tag{3.1}$$

where N_0 is the measured defect density at E_i. Since the interface traps are distributed in energy, decisions have to be made on which energy levels needed to be discretized. One extreme is to discretize the entire bandgap in small discrete energy intervals ΔE to account for all the trap states over the bandgap. Although this implementation gives the most accurate results, it is obvious that this method is computationally expensive, since for each discrete energy interval ΔE, a trap electron continuity equation needs to be added to the system for each interface node. On the other hand, if the bandgap is not discretized and the effect of interface trap states is implemented through the specification of some analytical representations, the simulation results will not be sufficiently accurate, since too many approximations would have to be made. In addition, the interface g-r simulation results will be no different than the approximate analytical results that have been shown in the previous published works in this area. Thus this approach defeats the purpose of implementing such mechanism to the simulator.

The best way to implement would be to discretize only at the energies that are critical to noise calculation, and at the same time keep the number of discrete energy intervals ΔE small to avoid any computational overhead. In addition, the effect of non-discretized trap levels needs to be accounted for. Choosing the right energy level to discretize requires some knowledge of how the g-r noise works. According to the classical g-r noise theory, the power spectral density due to carrier density fluctuation in a differential volume $\Delta\Lambda$ is given by

$$S_{\Delta\Lambda n_t} = \frac{4\tau}{1+\omega^2\tau^2} N_t f_t (1-f_t)\Delta\Lambda \tag{3.2}$$

where N_t is the trap defect density, τ is the trapping time constant, and f_t is the Fermi-Dirac (FD) distribution that determines the occupancy of traps. It can be shown from Equation (3.2) that the probability of carriers being trapped is proportional to the function $f_t(1-f_t)$. This function, plotted in Figure 3-2, is significant only at the electron quasi-Fermi level E_f at the interface and a few kT around it. The function becomes negligible at energies away from E_f, since those traps are either empty or filled, depending on the trap energy position. In addition, by integrating Equation (3.2) over the bandgap, the noise spectral density in $\Delta\Lambda$ can further be approximated as a delta function at E_f [15], since

$$\int_{E_v}^{E_c} N_t(E) f_t(1-f_t)\, dE \approx 4kTN_t\left(E_f\right) f_t\left(E_f\right)\left[1-f_t\left(E_f\right)\right] \tag{3.3}$$

From the arguments above, the need for discretizing the trap energy level at E_f for noise calculation is prominent. In addition, the approximation of taking only one discretized trap energy level is valid if the trap defect density for noise calculation at the discretized energy level is approximated by $4kTN_t\left(E_f\right)$.

One major difference between the implementations of the bulk and the interface g-r mechanisms is that for the interface, the trap energy level is not constant throughout the entire device, but it tracks with the quasi-Fermi level E_f at the interface. This means a proper dc steady state solution is needed at each interface node to identify its critical trap energy level before any interface noise simulation can be taken. Procedures to perform dc and noise simulations will be discussed in detail below.

3.3 DC and Noise Simulations

Although the traps at the energy levels other than E_f are not discretized, the trapped carriers at those levels induce a surface charge Q_{itf} at the interface that needs to be accounted for in the steady state condition. If the effect of the charge Q_{itf} is not included in the system, the solutions of ψ, n, and p at the interface will not be calculated correctly. This would introduce error to the value of E_f, forcing the simulator to discretize at a wrong trap energy level and result in faulty noise simulation results. Before any simulation, the traps at the interface first need to be characterized as either donor-like or acceptor-like. Assuming the interface traps to be acceptor-like, as shown in Figure 3-3, the interface charge can then be calculated as the product of the electron charge q and the trap carrier density $n_t(E)$ integrated over the bandgap

$$Q_{itf} = q\int_{E_v}^{E_c} n_t(E)\,dE \approx q\int_{Ev}^{Ec} N_t(E)\,f_t\left(E,E_f\right)dE \tag{3.4}$$

where $N_t(E)$ is the trap density described in Equation (3.1), and $f_t(E,E_f)$ is the FD distribution function. The expression Q_{itf} in this equation can be re-written as a function of n and p, which are the variables that the system is solving for. This is convenient since no new variable is needed. At the interface, the carrier transition rates described by the processes a, b, c, and d in Figure 3-2 are also needed to be set as a function of the quasi-Fermi level E_f, or a function of n and p, since the discretized trap energy level E_t moves with E_f. Because E_t lies at E_f, the Shockley densities are equal to

$$n_1 = n_i \exp\left[\left(E_f - E_i\right)/kT\right] = n \tag{3.5}$$

$$p_1 = n_i \exp\left[\left(E_i - E_f\right)/kT\right] = p \tag{3.6}$$

The rate equations characterizing the processes a, b, c, and d in the figure can then be written as

$$\begin{aligned} r_{n,itf} &= c_n n\left(N_t' - n_t\right) = c_n n\left[4kTN_o e^{\xi\left(E_f - E_i\right)} - n_t\right] \\ &= c_n n\left[4kTN_o\left(n/n_i\right)\right)^{\xi kT} - n_t\right] \end{aligned} \tag{3.7}$$

$$g_{n,itf} = c_n n_1 n_t = c_n n n_t \tag{3.8}$$

$$r_{p,itf} = c_p p n_t \tag{3.9}$$

$$\begin{aligned} g_{p,itf} &= c_p p_1\left(N_t' - n_t\right) = c_p p_1\left[4kTN_o e^{\xi\left(E_f - E_i\right)} - n_t\right] \\ &= c_p p\left[4kTN_o\left(n/n_i\right)\right)^{\xi kT} - n_t\right] \end{aligned} \tag{3.10}$$

respectively. Notice that the defect density N_t' at the discretized energy level is approximated as $4kTN_t(Ef)$. Equations (3.5) through (3.10) are only valid for the dc simulations. The pertinent equations at the interface are

$$F_\psi = -\frac{d^2\psi}{dr^2} - \frac{q}{\varepsilon}\left[p - n + N_D^+ - N_A^- - Q_{itf}\left(E_f\right) - n_{t,itf}\right] = 0 \tag{3.11}$$

$$F_n = \frac{dn}{dt} - \frac{1}{q}\nabla \cdot J_n + \left(r_{n,itf} - g_{n,itf}\right) - \gamma_{n,itf}\left(r,t,E_f\right) = 0 \tag{3.12}$$

$$F_p = \frac{dp}{dt} + \frac{1}{q}\nabla \cdot J_p + \left(r_{p,itf} - g_{p,itf}\right) - \gamma_{p,itf}\left(r,t,E_f\right) = 0 \tag{3.13}$$

$$F_{n_t,itf} = \frac{dn_{t,itf}}{dt} + \left(g_{n,itf} - r_{n,itf}\right) - \left(g_{p,itf} - r_{p,itf}\right) - \gamma_{t,itf}\left(r,t,E_f\right) = 0 \tag{3.14}$$

where $\gamma_{n,itf}$, $\gamma_{p,itf}$, and $\gamma_{t,itf}$ are the Langevin noise terms describing transition rate fluctuations. As mentioned earlier, for dc simulation the values of $r_{n,itf}$, $g_{n,itf}$, $r_{p,itf}$, $g_{p,itf}$ and Q_{itf} are functions of n and p. Once the dc solutions are obtained, the Shockley densities become constants as $n_1 = n_{dc}$ and $p_1 = p_{dc}$. The transition rates are then modified to the following for noise simulation

$$r_{n,itf} = c_n n\left(N'_{t,dc} - n_t\right) \tag{3.15}$$

$$g_{n,itf} = c_n n_1 n_t = c_n n_{dc} n_t \tag{3.16}$$

$$r_{p,itf} = c_p p n_t \tag{3.17}$$

$$g_{p,itf} = c_p p_1\left(N'_{t,dc} - n_t\right) = c_p p_{dc}\left[N'_{t,dc} - n_t\right] \tag{3.18}$$

For both the dc and noise calculations, the electron and hole capture coefficients for the discretized trap level still need to be specified.

3.4 Simulation Results

Interface noise simulations were carried out on a 0.45 μm nMOS structure. For the interface trap parameters, No is set to 10^{11} $\text{cm}^{-2}\text{eV}^{-1}$ [14], and both the electron and hole capture coefficients are set to 10^{-7} cm^3/s. A set of dc simulations is designed to test the response at the interface. The first simulation sets the drain, source, and substrate terminals to ground, and simulates with sweeping the gate bias voltage. The device is biased to act as a MOS capacitor. By increasing the gate bias voltage, more electrons move toward the surface. This shifts the Fermi level E_f toward the conduction band. At the same time, this increases the defect density at the discretized defect level. As expected, a higher trap carrier density nt,itf and a higher interface charge Q_{itf} are shown in the simulation results, plotted in Figure 3-4.

The second simulation sets the gate bias to a value above V_t to establish a channel under the gate. The trap carrier density at the interface nodes is observed as the bias V_{ds} increases. The results are plotted in Figure 3-5. As V_{ds} increases, electrons would move away from the surface near the drain, thus moving E_f closer to E_i and causing the trap carrier density to decrease. In the next test, the interface noise simulations are carried out for a few bias points. The preliminary results of the distributed current noise spectral density from the interface nodes under the gate are plotted in Figure 3-6. From these results, higher interface noise contributions from the interface nodes near the drain can be observed. Although the trap carrier density for those nodes is lower than at the interface nodes near the source, higher noise contributions must come from their higher scalar Green's function. Finally, the diffusion and interface g-r noise simulations are carried out simultaneously on the testing device operating from triode to saturation mode. The simulation results are shown in Figure 3-7. For the interface defect centers, the defect density is modeled by with an U-shaped energy distribution measured from either C-V or conductance data. The trap energy location of the discretized energy level is determined from the location of the Fermi level at the interface. Thus the only unknown variable is the capture coefficient. For the simulation results plotted in Figure 3-7, the capture coefficients for the interface traps were set to 10^{-7}cm^3/s. As the simulation results demonstrate, noise produced from the interface traps is negligible when compared to the diffusion noise. Simulations were also performed by varying the values of capture coefficients within reasonable physical range. Those results again have all shown negligible interface noise. This phenomenon is expected, since interface traps are generally considered to be fast trap states. Thus noise produced from these traps has a low magnitude at low frequencies and rolls off at high corner frequencies.

The conclusion of these simulations is that the g-r mechanism at the interface alone is not responsible for the low-frequency $1/f$-like noise that has been observed in MOS noise measurement data.

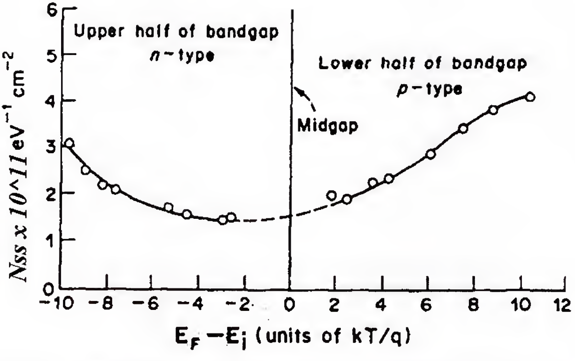

Figure 3-1. Measured trap density distribution from the conductance method [14]

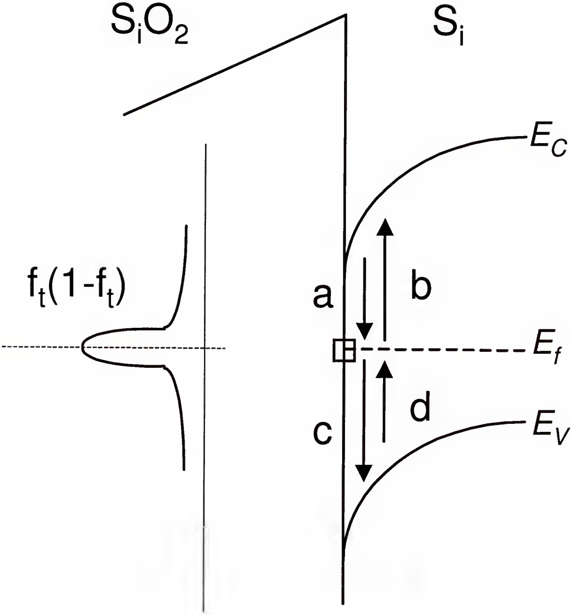

Figure 3-2. Energy band diagram at the interface, with the presence of a discretized trap energy level at E_f

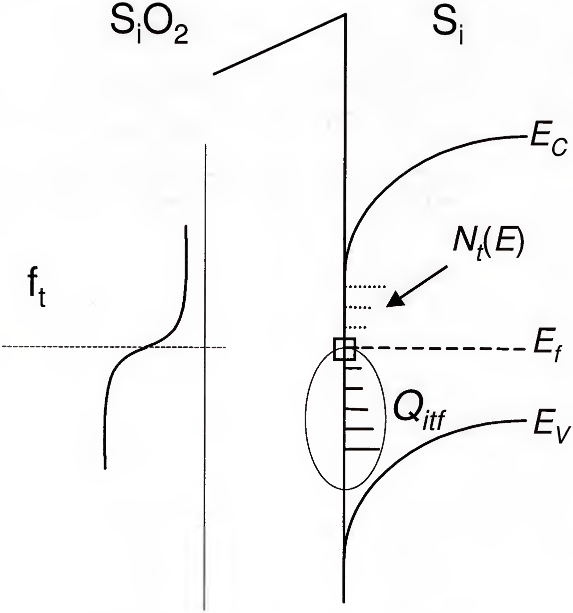

Figure 3-3. Trapped carriers at non-discretized trap levels induce a charge Q_{itf} at the interface

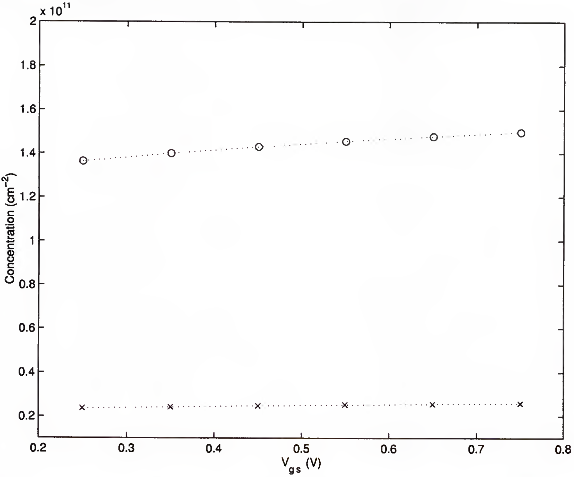

Figure 3-4. Interface trap carrier density $n_{t,itf}$(marked by "x") and interface charge Q_{itf}/q (marked by "o") for a V_{gs} sweep (V_{ds} and V_{bs} are set to zero)

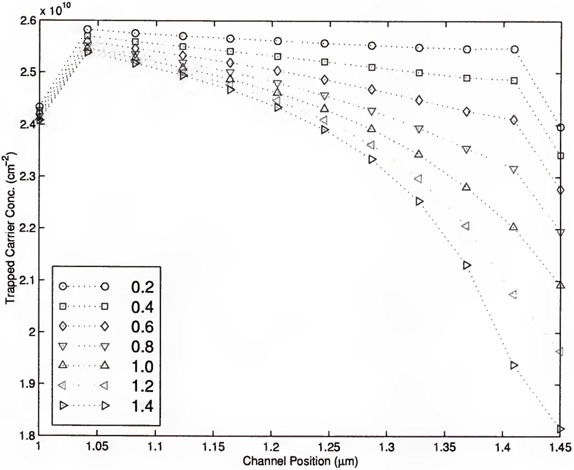

Figure 3-5. Interface trap carrier density $n_{t,itf}$ for a V_{ds} sweep. V_{gs} is set to a value greater than V_t and V_{bs} is set to zero.

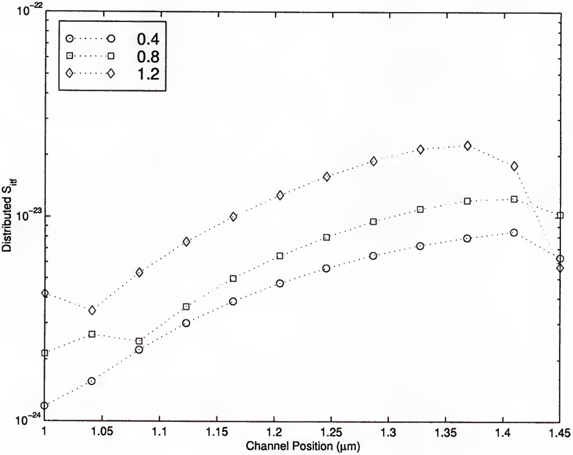

Figure 3-6. Distributed interface current noise spectral density for different V_{ds}. V_{gs} is set to a value greater than V_t and V_{bs} is set to zero.

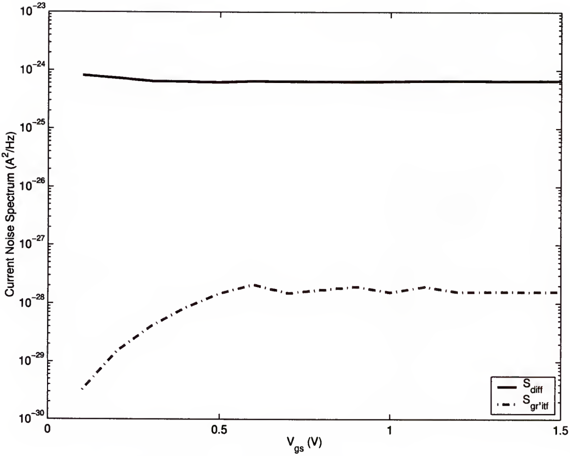

Figure 3-7. Various current noise spectral densities for a V_{gs} sweep (V_{ds} = 1.0 V)

CHAPTER 4
OXIDE TRAPPING NOISE

4.1 Introduction

The $1/f$-like noise in semiconductor devices has been studied extensively in the past. Most evidence has shown that its sources are located at or near Si/SiO_2 interfaces. This partially explains the fact that $1/f$-like noise is more dominant in MOS devices than in bipolar transistors, due to MOS structures having larger surface areas. According to McWhorter and others [3, 15, 16, 17, 18], $1/f$-like noise is the superposition of different Lorentzian spectra of which the corner frequencies spread across the low-frequency spectral window. The corresponding characteristic time τ of each Lorentzian spectrum, calculated from its corner frequency, gives information on the tunneling between defect centers in the oxide and at the interface. Even though the carrier tunneling mechanism between the traps in the oxide and at the interface is the source of $1/f$-like noise, only its macroscopic effect, represented by a characteristic time τ, is used in analytical derivations. Deriving the $1/f$-like noise mechanism from carrier tunneling equations and microscopic g-r trapping noise sources has not been attempted, due to the complexity of the problem. In recent years, device noise simulation packages have been implemented successfully into PDE-based device simulators. Utilizing the vector and scalar Green's functions calculated by the simulator, the noise at device terminals from each local noise source can be calculated. Simulations of diffusion, Hooge $1/f$, and bulk g-r noise have shown that none of these mechanisms can produce $1/f$-like noise. The bulk g-r mechanisms are fast processes with characteristic time constants too small to produce Lorentzian spectra at low frequencies. Surface noise, or so-called oxide trapping noise, has not been implemented until recently. The difficulty with the implementation of carrier tunneling mechanisms and oxide trapping noise is that carrier tunneling is not just dependent on variables at local grid points and adjacent points, but also depends on variables at grid points that are distant. The noise simulator needs to have a database to keep track of the link between each oxide point and its corresponding interface point. Recently, the carrier-tunneling mechanism and its associated noise was successfully implemented in FLOODS (FLorida Object-Oriented Device Simulator) [19, 20] and the oxide trapping noise simulation results show $1/f$-like characteristics as will be shown below.

4.2 Theory and Implementation

As stated previously, McWhorter's theory has been used frequently to explain the $1/f$ noise in MOS devices. Christensson [15] and others have proposed a "Tunneling and Capture" model, in which (i) the carriers first tunnel to a distance from the continuum states at the interface into the oxide, and then (ii) are captured by the traps that have the same energy level as E_f. This model is illustrated in Figure 4-1. As indicated in the figure, the electron needs to lose about 0.5 eV of energy to be trapped at the defect level. The validity of this model was later questioned, since measurement data did not support energy dissipation in the oxide [21]. The "Capture and Tunneling" model was later proposed by Fu and Sah [17] as the alternative for the previous proposed model. In this model, the carriers first get trapped by the fast defect centers at the interface through the Shockley-Read-Hall (SRH) process and then tunnel into the traps in the oxide at the same energy level, as illustrated in Figure 4-1. Thus the carriers do not dissipate energy in the oxide. The continuous trap distribution in energy over the bandgap at the interface is required to be the pre-existing condition. It is validated by measurement data, since large varieties of defects at the interface is a common characteristic of semiconductor devices. From this point forward, Fu and Sah's "Capture and Tunneling" model is used as the fundamental basis of the carrier trapping mechanism in the oxide.

4.2.1 "Capture and Tunneling" Model

Figure 4-1 shows the energy band diagram that illustrate the possible carrier transition processes at the interface and in the oxide [17]. Carriers in the continuum states can get trapped (process a & c) or de-trapped (process b & d) from the localized defect centers at the interface, through the SRH process. The trapped carriers can also communicate with defect centers that have the same energy level in the oxide through tunneling (process e & f). Since the trap centers at the interface and in the oxide are distributed in energy over the bandgap, discretization in energy is needed. In addition, both spatial and energy distributions of interface and oxide traps are needed. Measured data in the past [22] generally describes the trap distribution to be U-shaped in energy. Thus, it is modeled as [14]

$$N_t(E) = N_0 \exp[\xi \left|E - E_i\right|] \tag{4.1}$$

for simplicity. The term E_i is the intrinsic energy level. Discretization in small energy intervals would require a large number of trap electron continuity equations specified to the system. Thus carefully choosing the discretized energy level for noise simulation is critical. According to the g-r noise theory, the power spectral density due to a fluctuation in the number of trapped carriers n_t in a differential volume $\Delta\Lambda$, either from the trap centers at the interface or in the oxide, is [15, 18, 23]

$$S_{\Delta\Lambda n_t} = \frac{4\tau}{1+\omega^2\tau^2} N_t f_t (1 - f_t) \Delta\Lambda \tag{4.2}$$

where τ is the trapping time constant and f_t is the Fermi-Dirac distribution function. Plotting the function $f_t(1-f_t)$, which is a strong function of energy E, will display the critical energy levels where the contributions of the g-r noise are mostly coming from. As shown in Figure 4-1, this function is most significant at the electron quasi-Fermi level at the interface $E_{fn,i}$. By discretizing only the trap level at $E_{fn,i}$, the defect density in Eq. (4.2) is then modeled as $N_t' = 4kTN_t\left(E_{fn,i}\right)$, so that the function

$N_t f_t (1-f_t)$ can be represented as a delta function at $E_{fn,i}$ [15]. Since the discretized trap energy level E_t moves with $E_{fn,i}$, the Shockley densities are equal to

$$n_1 = n_i \exp\left[\left(E_f - E_i\right)/kT\right] = n \tag{4.3}$$

$$p_1 = n_i \exp\left[\left(E_i - E_f\right)/kT\right] = p \tag{4.4}$$

The rate equations characterizing the processes a, b, c, and d in Figure 4-1 then become

$$\begin{aligned} r_{n,itf} &= c_n n \left(N_t' - n_t\right) = c_n n \left[4kTN_o e^{\xi\left(E_f - E_i\right)} - n_t\right] \\ &= c_n n \left[4kTN_o \left(n/n_i\right)^{\xi kT} - n_t\right] \end{aligned} \tag{4.5}$$

$$g_{n,itf} = c_n n_1 n_t = c_n n n_t \tag{4.6}$$

$$r_{p,itf} = c_p p n_t \tag{4.7}$$

$$\begin{aligned} g_{p,itf} &= c_p p_1 \left(N_t' - n_t\right) = c_p p_1 \left[4kTN_o e^{\xi\left(E_f - E_i\right)} - n_t\right] \\ &= c_p p \left[4kTN_o \left(n/n_i\right)^{\xi kT} - n_t\right] \end{aligned} \tag{4.8}$$

respectively. The basic equations for the discretized energy level at the interface become

$$F_\psi = -\frac{d^2\psi}{dr^2} - \frac{q}{\varepsilon}\left[p - n + N_D^+ - N_A^- - Q_{itf}\left(E_f\right) n_{t,itf}\right] = 0 \tag{4.9}$$

$$F_n = \frac{dn}{dt} - \frac{1}{q}\nabla \cdot J_n + \left(r_{n,itf} - g_{n,itf}\right) - \gamma_{n,itf}\left(r,t,E_f\right) = 0 \tag{4.10}$$

$$F_p = \frac{dp}{dt} + \frac{1}{q}\nabla \cdot J_p + \left(r_{p,itf} - g_{p,itf}\right) - \gamma_{p,itf}\left(r,t,E_f\right) = 0 \tag{4.11}$$

$$\begin{aligned} F_{n_t,itf} = {} & \frac{dn_{t,itf}}{dt} + \left(g_{n,itf} - r_{n,itf}\right) - \left(g_{p,itf} - r_{p,itf}\right) \\ & - \gamma_{t,itf}\left(r,t,E_f\right) - \left(g_{ox} + r_{ox}\right) - \gamma_{ox}\left(r,t,E_f\right) = 0 \end{aligned} \tag{4.12}$$

where $\gamma_{n,itf}$, $\gamma_{p,itf}$, and $\gamma_{t,itf}$ are the Langevin noise terms describing transition rate fluctuations at the interface, and γ_{ox} is the Langevin noise terms associated with transition rate fluctuations through carrier tunneling. The terms g_{ox} and r_{ox} are the tunneling rates illustrated as processes e and f in Figure 4-1, respectively. These tunneling rates are functions of the tunneling coefficient T, the trap carrier density of the defect centers in the oxide $n_{t,ox}$, and the trap carrier density of the defect centers at the corresponding interface node $n_{t,itf}$

$$r_{ox}\left(x_i\right) = T n_{t,itf}\left(N_{t,ox} - n_{t,ox}\right)\Delta x \tag{4.13}$$

$$g_{ox}\left(x_i\right) = T\left(N_{t,itf} - n_{t,itf}\right) n_{t,ox}\Delta x \tag{4.14}$$

Notice that these rate equations are not just dependent on the local variables at the oxide node, but they are also dependent on the variables at the interface. From a simple classical tunneling model [15, 21, 14, 24] with a constant barrier height, the tunneling coefficient is given by

$$T = T_0 \exp\left(\alpha d\right) \tag{4.15}$$

where $\alpha = -2\sqrt{2m_{ox}\phi_{itf}/\hbar^2}$ is the attenuating constant of the wave function in the oxide associated with the barrier height ϕ_{itf} at the interface. In addition to the basic equations above, the equations to be simulated for an oxide node at position x_i are the Poisson and trap electron continuity equations

$$F_{\psi_{x_i}} = -\frac{d^2\psi_{x_i}}{dr^2} - \frac{q}{\varepsilon}\left[-\frac{Q_{ox}\left(x_i, E_f\right)}{q} - n_{ox}\left(x_i, E_f\right)\right] = 0 \tag{4.16}$$

$$F_{ox} = \frac{dn_{ox}\left(x_i, E_f\right)}{dt} - r_{ox} + g_{ox} - \gamma_{ox}\left(x_i, t, E_f\right) = 0 \tag{4.17}$$

4.2.2 Modeling of the Defect Density in Oxide

One of the main goals of this research work is to characterize the defect density distribution in the oxide region of semiconductor devices. Knowledge of the defect density distribution is critical for the operation of a MOSFET, since defects play important role in gate leakage current and act as the source of low frequency noise. Different models for the oxide defect density can be applied to the simulator to compare the simulation data with the measured noise results. Thus an optimal defect density profile can be obtained once a match between simulations and measurements is found via reverse engineering.

Research in the past speculates that the defect density in the oxide varies in position and in energy, based on observations such as the ones listed below:

- As stated previously, the measured interface trap density is found to have a U-shape in energy. For the same reason that more defect centers are found near the continuum states, one can assume that the traps in the oxide have a U-shape in energy distribution also.
- From a simple classical tunneling model, the tunneling rate is an exponential function of the distance between the interface and the oxide traps, as stated in Eq. (4.15), if each tunneling carrier sees a constant barrier height. It can be shown analytically that the tunneling rate calculated with this simple model leads to the ideal $1/f$ noise spectrum, with the condition that the defect density in the oxide has to be constant in energy and space. For this reason, many in the past model the defect density in the oxide with a constant value, for simplicity in analytical noise derivations and for the modeling of $1/f$ noise observed in measurements.
- Defects are accumulated at or near the interface. It has been reported from noise measurements that the logarithmic slope of $1/f$-like noise deviates from -1, as the frequency increases in the spectral window. This type of noise is sometimes called as "pseudo $1/f$ noise". Again by modeling the tunneling rate as a function of distance and with a constant barrier height, the measurement data supports the theory of an increasing defect density distribution at the regions near the interface in the oxide. Depending on the location of the defects, for those that have a higher defect density near the interface, their effect would only be shown at high frequencies, since they are very close to the interface and the tunneling rates for the carriers communicating with them are fast.

Based on the observations described here, Celik and Hsiang [14] came up with an analytical expression for the oxide defect density as a function of energy and distance from the interface. In addition, the expression accounts for band bending in the oxide. The defect density is modeled as

$$N_t(E,x) = N_0 \exp\left[\xi (E - E_i) + \frac{q\lambda (V_g - V) x}{t_{ox}} + \eta x\right] \tag{4.18}$$

where $q(V_g - V)x/t_{ox}$ is the amount of band bending at a distance x away from the interface. Based on their noise measurements on MOS devices, they found

$N_o = 4 \cdot 10^{17}$ cm^{-3}eV^{-1}, $\xi = 3.1$ eV^{-1}, $\lambda = 62$ eV^{-1}, and $\eta = 4.5 \cdot 10^{7}$ cm^{-1}. Ideally, the band-bending factor λ should be equal to unity, since it is more physical for the defect density to be modeled by the exact amount of band bending at each location, without this multiplication factor. However, the published value of λ provides a better match between their measured and calculated data.

4.2.3 Modeling of the Carrier Tunneling Rates

In general, the carrier tunneling rate is represented by

$$T = T_0 \exp(\alpha d) \tag{4.19}$$

where the attenuation constant of the wave function depends on the shape of the barrier. It also depends on the effective mass of the carrier in the oxide, and the barrier height at the interface ϕ_{itf}. There are two general models that can be used to characterize carrier tunneling. The simplest one is the square barrier tunneling (SBT) model. As the name implies, the carrier sees a square potential barrier before tunneling. Of course this is only true under flat-band condition. Due to the simplicity of the SBT model, it is widely used as an approximation for calculating the tunneling characteristic time constant in analytical derivations of noise theory. In this model, the attenuation constant is defined as

$$\alpha = -\frac{2}{\hbar}\sqrt{2m_{ox}\phi_{itf}} \tag{4.20}$$

Setting $m_{ox} = 0.4m_o$ as obtained from BSIM's parameter set [25], α is then equal to $1.303 \cdot 10^{8}$ cm^{-1} with $\phi_{itf} = 4.05$ eV. In the actual simulation α will not be a constant, since it is a function of the barrier height ϕ_{itf} which depends on the location of the Fermi level. In the second model the tunneling carrier sees a trapezoidal potential barrier, a situation found in MOSFETs. To calculate the tunneling rate, both the barrier heights at the interface ϕ_{itf} and at the trap location in the oxide ϕ_{ox} are required, as stated in the following expression

$$\alpha = -\frac{4}{3}\frac{\sqrt{2m_{ox}}}{\hbar}\frac{\phi_{itf}^{3/2} - \phi_{ox}^{3/2}}{\left(\phi_{itf} - \phi_{ox}\right)} \tag{4.21}$$

As $\left(\phi_{itf} - \phi_{ox}\right)$ approach zero, the value α in Eq. (4.21) approaches the one in Eq. (4.20).

As mentioned previously, the tunneling rate equations specified as Eq. (4.13) and (4.14) rely on non-local variables. The effect of tunneling from any oxide node to each interface node, and vice versa, needs to be examined. One specific behavior of carrier tunneling is that the tunneling rates are highly dependent on the tunneling probability, which is an exponential function of position and distance. One approximation to take is to assume that the traps at each oxide node are most likely to interact with their closest interface node. This would require a mapping table to inform the simulator which interface nodes should be linked with the oxide nodes that are considered. The components of the Jacobian matrix can then be modified as follows

$$J = \begin{bmatrix} & \vdots & & \vdots & \\ \cdots & \frac{dF(n_{ox})}{dn_{ox}} & \cdots & \frac{dF(n_{ox})}{dn_{itf}} & \cdots \\ & \vdots & & \vdots & \\ \cdots & \frac{dF(n_{itf})}{dn_{ox}} & \cdots & \frac{dF(n_{itf})}{dn_{itf}} & \cdots \\ & \vdots & & \vdots & \end{bmatrix} \tag{4.22}$$

4.3 Verification with Analytical Expressions

To illustrate the oxide trapping noise simulation package in FLOODS, a 0.4 μm n-channel MOSFET structure with a gate oxide thickness of 140 Å is chosen for testing. The noise simulation is compared with the analytical expression for $1/f$ noise in MOSFETs to determine the accuracy of this tool. In FLOODS, the oxide defect density of any testing device structure can be specified in the form of Eq. (4.18) proposed by Celik and Hsiang [14]. Thus, if FLOODS input parameters for noise calculation are properly adjusted to include only the physics that was considered in Celik and Hsiang's derivation, comparisons between the FLOODS simulation outcome with their theoretical expectation can then be judged. Under the assumption of an oxide defect density $N_t(E,x) = N_0 \exp[\xi(E-E_i)]$ and with the square barrier tunneling model to characterize the transition of carriers between the traps at the interface and in the oxide, the current noise spectral density at the drain terminal can be expressed as [18]

$$S_{I_d} = \frac{W\mu^2 q^2 kTN_0}{2L^3 f\alpha\gamma}\left(\frac{n_{0_s}}{n_i}\right)^{\gamma} V_d\left(2V_{d,sat}-V_d\right)\left[1-\frac{\left(V_{d,sat}-V_d\right)^{\gamma}}{V_{d,sat}^{\gamma}}\right] \tag{4.23}$$

where $V_{d,sat} = V_{gs} - V_T$, $\gamma = \xi kT$, and n_{0_s} is the surface electron concentration at the source. S_{I_d} of Eq. (4.23) is plotted in Figure 4-2 against the simulation results, and excellent agreement is shown in the figure for the data in the linear region.

In the past the $1/f$ noise was explained analytically for the MOS device operating in the linear mode of operation only. The transfer function for coupling the noise from each noise source was derived from the gradual channel approximation (GCA) and the derivation was simplified to a one-dimensional problem. Also, strong inversion is assumed. Therefore, the $1/f$ noise formulation breaks down in saturation and in sub-threshold operating regions. This is not the case when it is simulated in the PDE-based simulator, where the proper transfer function can be computed numerically at each grid point, in either the sub-threshold, linear, or saturation modes of operation. At low drain bias, noise simulations are performed with a frequency sweep. The results are plotted in Figure 4-3. As expected, oxide trapping noise is a pure $1/f$ noise with a corner frequency in the MHz range. Taking a cross-section of the distributed current noise spectral densities of the oxide trapping noise at a point half way between the drain and source regions, data obtained at each frequency point, a decade apart, is plotted in Figure 4-4. It is shown in this figure that the first line from the left corresponding to the lowest frequency (1 Hz) peaks around 22 Å away from the interface. At the next frequency (10 Hz), the overall magnitude of the current noise spectral density decreases, and at the same time the peak moves closer to the interface. With this figure, one can identify the contributions of the noise produced in each region of the oxide at any specific frequency, thus one is able to identify the critical noise region and how far it is away from the interface. An example of the distributed current noise spectral density is shown in Figure 4-5.

To observe the changes in oxide trapping noise in different regions of device operation, the distributed current noise spectral density in the oxide is plotted under different drain bias conditions. As stated previously, a square barrier tunneling model with a defect density distribution independent of position is used for testing. In this model the tunneling rates and the characteristic time depend only on distance. This allows the peak of the distributed current noise spectral density to be located at the same distance away from the interface at each specific frequency. Once the critical distance is identified for the chosen frequency, the distributed current noise spectral density of a cross-section along the channel under different drain bias is plotted, as shown in Figure 4-5 and Figure 4-6. Under the linear mode of operation, noise contributions at each region along the channel increase as V_{ds} increases. The area under the curve reaches the maximum when the drain bias V_{ds} equals $V_{d,sat}$. As the drain bias is increased further, the peak of the ridge shifts toward the source, the same way the channel pinch off region relocates. Yet the area under the curve, which is a measure for the noise observed at the contacts, stays the same when compared with the curve corresponding to $V_{ds} = V_{d,sat}$.

No significant difference to noise performance was found by switching the tunneling mechanism from the square barrier tunneling model to the trapezoidal tunneling model. The main reason for such an insignificant change is that for this device with a gate oxide thickness of 140 Å, with a gate bias of 1.0 V, the effect of band bending at the locations where low frequency noise is significant is quite small.

Thus the trapezoidal barrier seen by the tunneling carriers looks almost like a square barrier.

As mentioned in the previous chapter, the interface g-r noise source is negligible when compared with the velocity fluctuation or the oxide trapping noise. Thus the interface parameters, such as the interface capture coefficients c_n and c_p and the interface defect density $N_{T_{itf}}$, cannot be extracted from noise measurement data. In addition, the interface trap centers serve only as stepping stones for the carriers in the channel to reach the trap centers in the oxide, and the carrier transition is dominated by the carrier tunneling rates g_{ox} and r_{ox} defined in Equations (4.13) and (4.14). Thus, changing the values of the interface parameters c_n and c_p and $N_{T_{itf}}$ does not alter the simulated oxide trapping noise outcome, as long as those parameters ensure that the carrier transition rates $r_{n,itf}$, $g_{n,itf}$, $r_{p,itf}$, and $g_{p,itf}$ are always higher than the tunneling rates g_{ox} and r_{ox}. In the example shown in this section, we used 10^{-7} cm^3/s and 10^{11} cm^{-2}eV^{-1} for the interface capture coefficients and the interface defect density, respectively. The parameter which determines the curvature of the U-shaped trap distribution in energy is set to $\xi = 3.1$, as determined from the result of the conductance method [14, 18].

4.4 Noise Spectroscopy

Motorola supplied us with the device structure, doping profile, and measurement data of a 0.45 μm graded channel MOS (GCMOS) transistor. In this device, a boron-doped implant is present near the source region, as shown in Figure 4-7. Both the device structure (such as the non-planner oxide thickness) and the doping profile were calibrated through inverse engineering from the measured I-V and C-V data. Once the initial device structure and doping profile from the calibration were obtained, all oxide regions of the device were re-gridded with fine mesh grids. A prerequisite for accurate oxide trapping noise simulation is to have dense grid points in the oxide meshes near the interface, hence the characteristics of the noise parameters that vary strongly with distance, such as the carrier tunneling rate, can be accounted for properly.

As mentioned previously, the interface parameters do not effect the oxide trapping noise outcome, as long as the interface carrier transition rates are faster than the carrier tunneling rates. Thus, for Motorola's GCMOS transistor the interface parameters for simulating the oxide trapping noise are set to $c_n = c_p = 10^{-7}$ cm^3/s and $N_{T_{itf}} = 10^{11}$ cm^{-2}eV^{-1}. The defect density in the oxide is modeled according to Equation (4.18), where the parameters are set to $\xi = \lambda = 3.1$ and $\eta = 0$. For the carrier tunneling rate, the attenuation constant α is modeled by Equation (4.21) instead of (4.20) for better accuracy.

Measured noise is plotted in Figure 4-8. The data was taken when the device was biased with a constant $V_{ds} = 2.0$ V and sweeping V_{gs} from 0.4 to 0.9 V. Since the threshold voltage V_t extracted from both the measured and simulated characteristic I-V data is 0.566V, the measurement has covered both the subthreshold and inversion modes of operation of the device. To analyze the excess noise, each set of data for any specific gate bias voltage is decomposed into two parts: the background pure $1/f$ noise component, and the visible g-r Lorentzian spectra. We speculate that the Lorentzian spectra visible above the background $1/f$ noise stem from discrete defects in the oxide. The background pure $1/f$ noise for each gate bias is represented by a solid line in Figure 4-8.

To analyze the background $1/f$ component, simulations were carried out to find the constant N_0 that could produce the noise which has the best fit to the measured data. We discovered that for this device, the critical noise region is not in the gate oxide above the center or near the drain region of the channel like the example shown in the previous section, but is in the smile oxide directly above the graded channel boron-doped implant near the source region, as the distributed current noise spectral density plotted in Figure 4-9 illustrates. Even though the peak of the distributed noise moves horizontally (parallel to the y axis) with the changing drain bias voltage and moves vertically (parallel to the x axis) with different frequency, the peak is always confined to the oxide area above the graded channel doping, indicated in Figure 4-7. This phenomenon can be explained by a strong scalar Green function from the noise critical region to the drain contact, due to the presence of the graded channel doping.

Studying the results of the simulations led to the conclusion that the parameter N_0 of oxide defect modeling in Eq. (4.18) cannot be limited to a constant value. Thus we modeled it as a function of the position y. In order to get the simulation data to match the measured noise data for a wide range of gate bias values, as shown in Figure 4-10, the parameter N_0 in the oxide noise critical region needs to be modeled by the function shown in Figure 4-11. This result demonstrates that the defect density in the smile oxide is strongly related to its thickness. As derived from the measured noise data, the defect density is higher when the smile oxide is thicker, as illustrated in Figure 4-12.

Figure 4-10 shows that there is a discrepancy between the simulated and measurement data for V_{gs} = 0.4 V. We suspect that the measured noise at that bias is not the true device noise, but is influenced by the noise introduced from the measurement setup. As the simulation indicates, the critical noise region for the gate biases V_{gs} = 0.4 V and V_{gs} = 0.5 V are close enough, that we expect that the same discrete defect centers causing the Lorentzian spectra observed in the noise for V_{gs} = 0.5 V would also show up in the noise for V_{gs} = 0.4 V. But an elevated pure $1/f$ noise component was observed instead, as shown in Figure 4-8.

To observe the Lorentzian spectra in the measured noise, the function $S_I \times f$ vs. f is plotted in Figure 4-13. From this figure we identify three major Lorentzian spectra, marked by a, b, and c, that spread among the five sets of measured data. To approximate these spectra, three discrete defect centers, α, β, and γ, are placed inside the oxide noise critical region, shown in Figure 4-14, to produce the Lorentzian spectra at a, b, and c in the spectral window, respectively. By adjusting each defect center's location and magnitude, we obtain a reasonably good agreement between experiment and simulation, as illustrated in Figure 4-13. A problem with the discrete defect distributions is that they may spread into more data sets than was intended. For example, the discrete defect distribution α, which intends to add a Lorentzian spectrum near 10^2 Hz for noise measured at V_{gs} = 0.8~0.9 V, has unintentionally elevated the simulated noise at the same frequency at lower gate biases. With denser grid spacing and more iterative steps to model the shape of the discrete defect profiles, one can achieve a better match between the simulated and measurement data.

4.5 Summary

The advantage of implementing the carrier-tunneling mechanism and oxide trapping noise into a PDE-based simulator is that one is able to observe how the $1/f$-like surface noise sources are distributed in the oxide and at the interface. Thus one can pinpoint the critical noise producing region. In addition, the relationship between device surface quality and the $1/f$-like noise can be simulated. Comparing the measured and simulated noise data, oxide and interface defect density can be estimated accurately. This information can be used to predict device lifetime and estimate leakage current through the gate oxide. The oxide trapping noise simulation can also be used to analyze $1/f$-like noise for MOS devices operating in the saturation mode. This cannot be done analytically, due to the 2-dimensional complexity of the channel layout and carrier flow patterns.

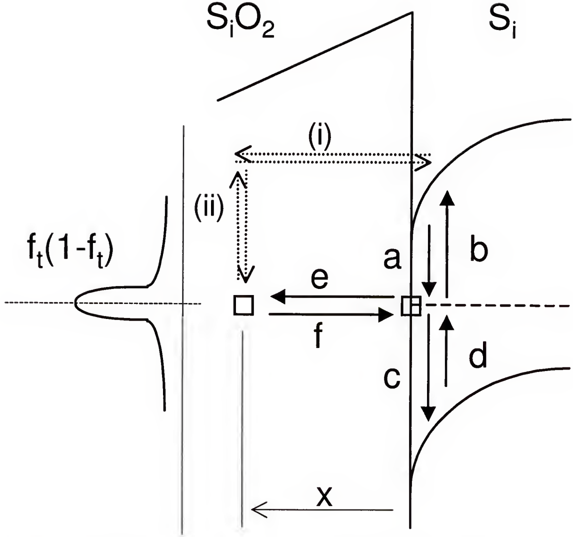

Figure 4-1. “Tunneling and Capture” and “Capture and Tunneling” models

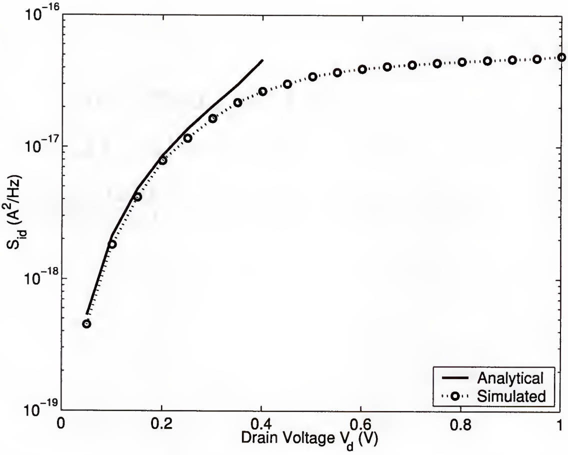

Figure 4-2. Simulation results are plotted and compared with the analytical prediction.

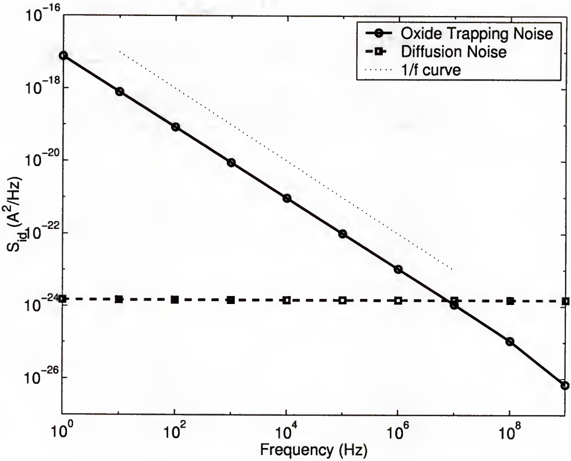

Figure 4-3. Current noise spectral density vs. frequency

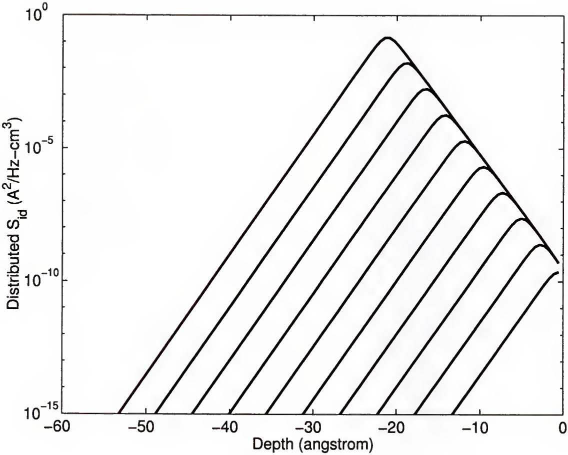

Figure 4-4. Distributed current noise spectral density for different frequencies

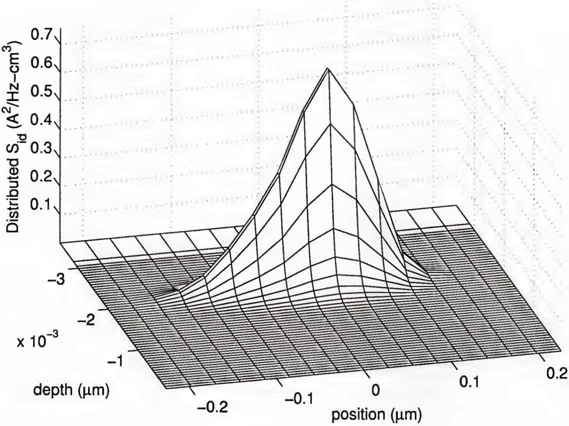

Figure 4-5. Distributed current noise spectral density along the channel for V_{gs} = 1.0 V and V_{ds} = 0.45 V (f = 1 Hz)

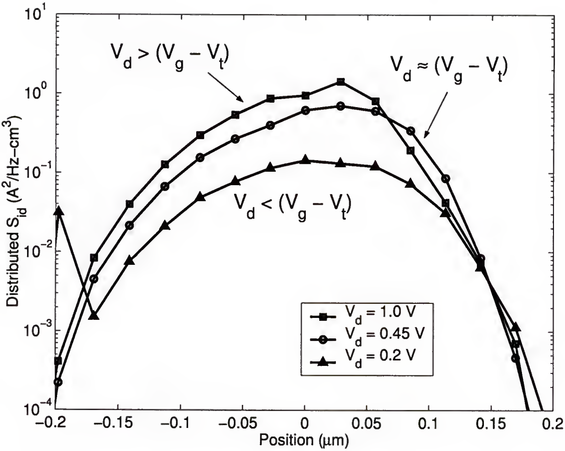

Figure 4-6. Distributed current noise spectral density along the channel for different bias conditions

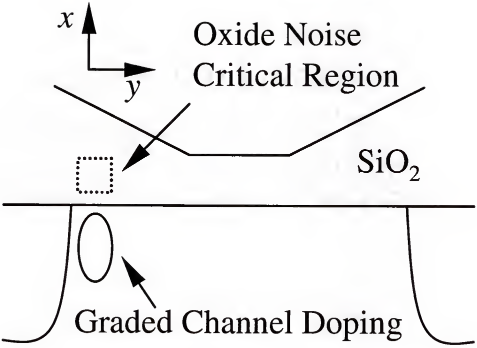

Figure 4-7. Device structure of a 0.45 μm graded channel MOS transistor

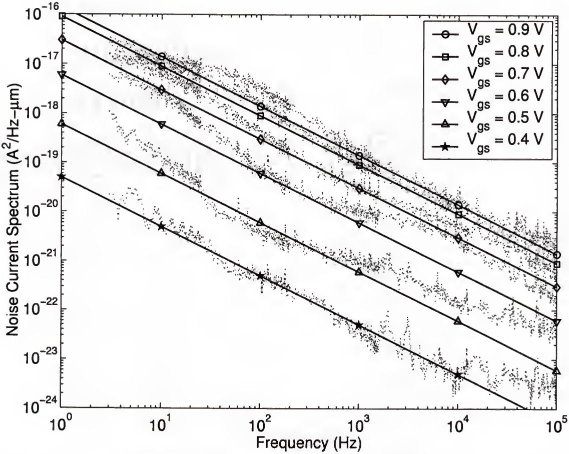

Figure 4-8. Measured current noise spectral density as a function of V_{gs} and frequency. The drain bias V_{ds} = 2.0 V. The solid lines represent the simulated background pure $1/f$ noise components.

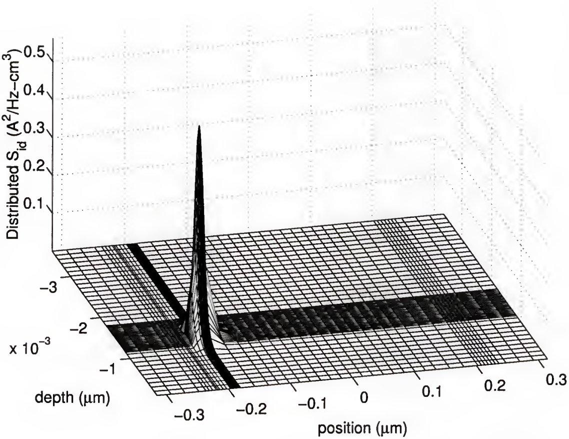

Figure 4-9. Distributed current noise spectral density for f = 25 Hz. The bias values of the device under simulation are V_{ds} = 2.0 V and V_{gs} = 0.8 V. The oxide region is shown with x = 0 to be the midway between the metallurgical source and drain junctions.

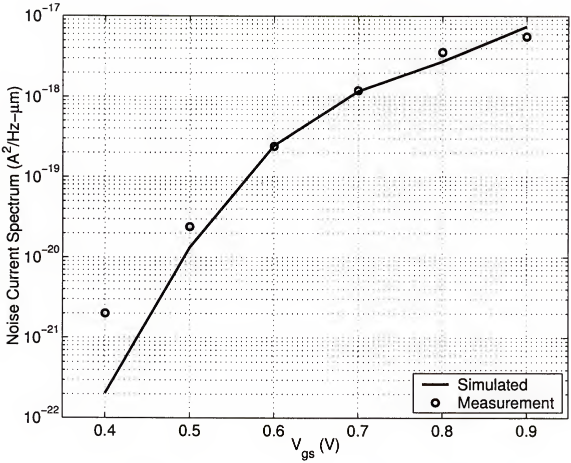

Figure 4-10. Comparison between the simulated and measured data of the pure 1/f noise component (V_{ds} = 2.0 V, f = 25 Hz).

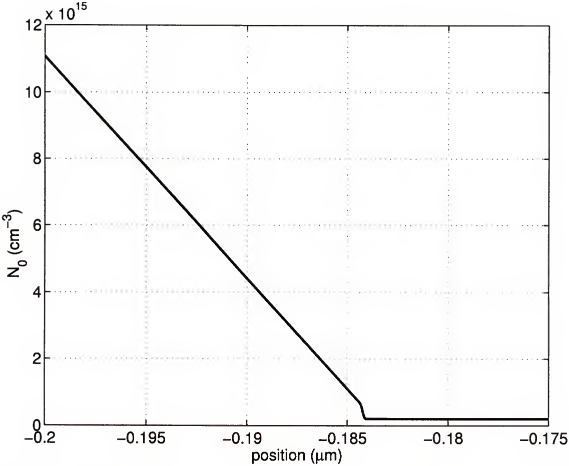

Figure 4-11. Profile of the defect density parameter N_0 as function of position parallel to the channel. Note that only the parameter in the oxide noise critical region indicated in Figure 4-7 is shown here.

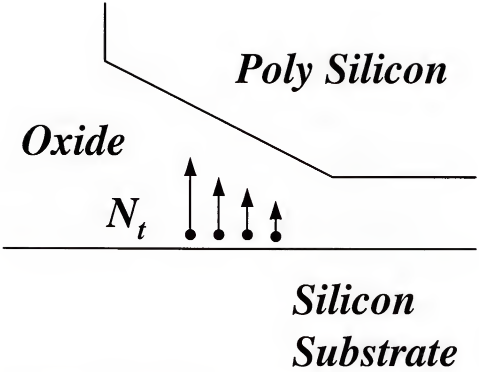

Figure 4-12. Defect density profile in the smile oxide

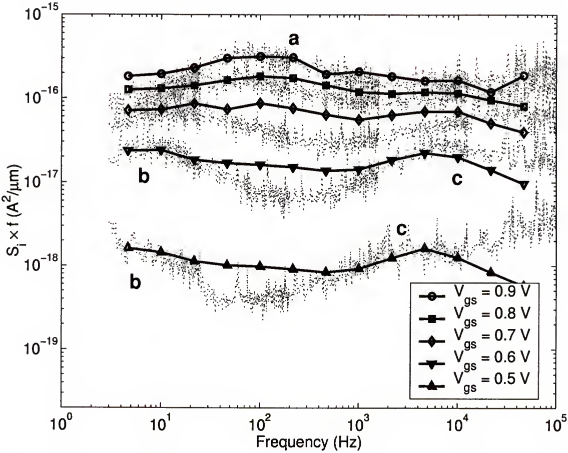

Figure 4-13. Product of current noise spectral density and frequency to identify Lorentzian spectra in the measured and simulation data

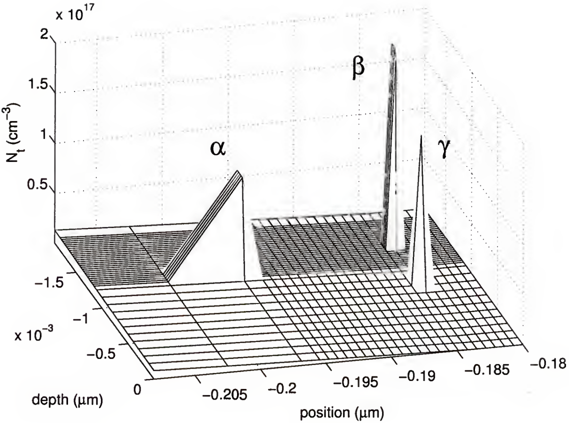

Figure 4-14. Discrete defect distributions responsible for the Lorentzian spectra observed in the experiment. Note that only the distributions in the oxide noise critical region indicated in Figure 4-7 are shown here.

CHAPTER 5
MAXIMUM ALLOWABLE BULK DEFECT DENSITY FOR GENERATION-RECOMBINATION NOISE FREE OPERATION OF n^+-n-n^+ STRUCTURES

5.1 Introduction

Many defects that exist in semiconductor devices are often unintentional. Elements such as Carbon, Oxygen, and various metals may be introduced to the wafer during processing steps, and then become carrier trap centers that affect device performance and produce generation-recombination (g-r) noise. The g-r noise is due to the random fluctuations in the trapping and de-trapping rates in the defect trap centers in the forbidden band gap. This in turn causes the current or the voltage, depending on the condition at the contact terminal, to fluctuate as well. The generation and recombination transition has generally been characterized by the Shockley-Read-Hall model. In this model, each defect species is specified by its defect density, its carrier capture coefficients, and its energy position relative to either the conductance or valence band. As has been shown in the past, g-r noise offers a unique opportunity to experimentally determine these trap parameters on as-made devices under actual bias conditions. An advantage of the g-r noise trap spectroscopy over other defect spectroscopy tools is that only defects that affect device performance, via their noise contributions, are probed [26]. The focus of this paper however is to study the maximum allowable bulk defect density to guarantee g-r noise free operation under all bias conditions of specifically two terminal drift dominated devices which are known to be sensitive to bulk defects. Having this information may guide the decision on the need for incorporating defect reduction steps in the device fabrication process. Both the local g-r noise strength and the transfer Green's function, which couples the carrier fluctuations in each differential volume of the device to a specific contact, change with bias. The simple analytical model of g-r noise indicates that the current noise spectral density of a bulk resistor in the ohmic regime is proportional to I^2 or E^2, where I is the current and E is the electric field in the device. As a consequence, increasing the bias across a device will nearly always lift a g-r noise component out of the thermal noise background. In practice however, carrier heating and space charge injection from the contacts will lead to field dependent carrier mobilities and position dependent carrier densities resulting in a decrease of the g-r noise signature of a defect center at high bias to values possibly below the velocity noise level. It is difficult to unravel the full physical noise picture analytically. We therefore expanded the capabilities of a semiconductor device simulator with g-r and velocity fluctuation noise models to account for these effects.

5.2 Implementation

The g-r process can be described by the Shockley-Read Hall model, as shown in Fig. 1. For illustration purposes, assume there is one defect trap level in the bandgap, and the traps are acceptor-like. In addition to the three basic Shockley equations

$$F_\psi = -\frac{d^2\psi}{dr^2} - \frac{q}{\varepsilon}\left[p - n + N_D^+ - N_A^- - n_t\right] = 0 \tag{5.1}$$

$$F_n = \frac{dn}{dt} - \frac{1}{q}\nabla \cdot J_n - g_n + r_n - \gamma_n = 0 \tag{5.2}$$

$$F_p = \frac{dp}{dt} + \frac{1}{q}\nabla \cdot J_p - g_p + r_p + \gamma_p = 0 \tag{5.3}$$

a trapped electron continuity equation is added to describe the carrier density fluctuations at the trap level E_T

$$F_{n_t} = \frac{dn_t}{dt} + g_n - r_n - g_p + r_p - \gamma_t = 0 \tag{5.4}$$

where γ_n, γ_p, and γ_t are the Langevin noise terms describing random transition rate fluctuations. The transition rates can be expressed as

$$r_n = c_n n \left(N_T - n_t\right) \tag{5.5}$$

$$g_n = c_n n_1 n_t \tag{5.6}$$

$$r_p = c_p p n_t \tag{5.7}$$

$$g_p = c_p p_1 \left(N_T - n_t\right) \tag{5.8}$$

where N_T represents the defect density and n_1 and p_1 are the Shockley parameters defined as

$$n_1 = N_C \Im_{1/2}\left(\frac{E_T - E_C}{kT}\right) \approx N_C \exp\left(\frac{E_T - E_C}{kT}\right) \tag{5.9}$$

$$p_1 = N_V \Im_{1/2}\left(\frac{E_V - E_T}{kT}\right) \approx N_V \exp\left(\frac{E_V - E_T}{kT}\right) \tag{5.10}$$

with the assumption that the trap level is at least a few kT from the conductance and valence band edges and other symbols have their usual meaning. In these equations the defect species are specified by three parameters: trap energy level (E_T), trap density (N_T), and capture coefficients (c_n, c_p).

Physics based noise models are implemented into the device simulator using the impedance field method (IFM) [4]. Two elements are required to calculate the noise at the contact terminals. The first is the magnitude of the microscopic noise sources $K_{\gamma_\alpha,\gamma_\beta}$ (where $\alpha, \beta = n, p, n_t$) at each grid point, represented by the added Langevin noise terms in the partial differential equations (PDE) in (5.2)-(5.4). For the g-r noise sources, the microscopic noise sources $K_{\gamma_\alpha,\gamma_\beta}$ are derived from the Poisson process and are given by [11]

$$\begin{aligned} K_{\gamma_n,\gamma_n} &= 2g_n + 2r_n = -K_{\gamma_n,\gamma_t} \\ K_{\gamma_p,\gamma_p} &= 2g_p + 2r_p = -K_{\gamma_p,\gamma_t} \\ K_{\gamma_t,\gamma_t} &= K_{\gamma_n,\gamma_n} + K_{\gamma_p,\gamma_p} \end{aligned} \tag{5.11}$$

The second element is the transfer function that couples the perturbation of the PDEs from each grid point to the device terminals. The scalar Green's transfer function $\tilde{G}$ for each carrier type at each node is obtained by perturbing the PDE associated with the carrier at the node, and then observing the changes at the contact terminals. The g-r noise current spectral density at an external contact terminal is calculated through the following expression [4]

$$S_{I,gr} = \sum_{i=1}^{N_{trap}} \sum_{\alpha,\beta=n,p,n_t} \int_{vol} \tilde{G}_\alpha K_{\gamma_\alpha,\gamma_\beta} \tilde{G}_\beta^* dr \tag{5.12}$$

where N_{trap} is the number of trap levels in the device.

The g-r noise mechanism described above was implemented into FLOODS (Florida Object-Oriented Device Simulator). FLOODS is a PDE-based, generalized box scheme device simulator. The implementation of velocity fluctuation noise is described in an earlier paper [6].

5.3 Simulation

Extensive research on bulk g-r noise for either single or multiple defect trap systems [11, 12] has shown that the noise spectrum of the number of trapped carriers N_t in a small differential volume Δv equals

$$S_{\Delta N_t,\Delta v}(f) = \frac{S_{\gamma_t}\tau_t^2}{1+\omega^2\tau_t^2} \tag{5.13}$$

where $\omega = 2\pi f$. The spectrum of γ_t is equal to

$$S_{\gamma_t} = \lim_{\tau\to\infty} 2\tau\overline{\gamma_t\gamma_t^*} = 2\left(g_n + r_n + g_p + r_p\right) \tag{5.14}$$

where the units of γ_t, and the generation and recombination rates have been changed into number of carriers per second for the remainder of this paper. Combining (5.13,5.14) results in

$$S_{\Delta N_t,\Delta v}(f) = \frac{2\left(g_n + r_n + g_p + r_p\right)\tau_t^2}{1+\omega^2\tau_t^2} \tag{5.15}$$

The value of the low frequency plateau is

$$S_{\Delta N_t,\Delta v}(f \to 0) = 2\left(g_n + r_n + g_p + r_p\right)\tau_t^2 \tag{5.16}$$

To simulate bulk defect noise properties, a 2-D n^+-n-n^+ bulk resistor was created. The n- and n^+-region are doped with N_d = 10^{15} and N_{d+} = 10^{18} cm^{-3} donors, respectively. The length of the n-region L is 2 μm, and the n^+-regions are 0.5 μm long in length on each side of the device. The cross-sectional area A is 1 μm^2. A defect center E_T at E_F = (E_C - 0.265 eV) is chosen for the simulation. This choice was guided by the fact that trap levels close to E_F produce maximum noise levels [6] and thus represent a worst case scenario. Electron and hole capture coefficients, c_n and c_p and defect density N_T are set to 10^{-8} cm^3/s (typical values) and , initially, 10^{12} cm^{-3}, respectively. Since E_T is much closer to E_C than E_V, one can safely assume $g_n, r_n >> g_p, r_p$ and $g_n \approx r_n$. Eq. (5.15) above then simplifies to

$$S_{\Delta N_t,\Delta v} = \frac{4 r_n \tau_t^2}{1+\omega^2\tau_t^2} = \frac{4 g_n \tau_t^2}{1+\omega^2\tau_t^2} \tag{5.17}$$

With

$$S_{\Delta N_t} = S_{\Delta N} \tag{5.18}$$

where ΔN is the number of carriers in the conduction band in the differential volume and integrating (5.17) over device volume, the current spectral density of the resistor in the ohmic regime becomes

$$S_I(f) = \frac{I^2}{N^2} S_{\Delta N}(f) = \frac{4 I^2 g_n \tau_t^2}{(LAn)^2} \cdot \frac{1}{1+\omega^2\tau_t^2} \tag{5.19}$$

where we used

$$\frac{S_N}{N^2} = \frac{S_V}{V^2} = \frac{S_I}{I^2} \tag{5.20}$$

The symbols V and I are the dc bias voltage and current, respectively, and N represents the total number of carriers in the device. Since $c_n(n+n_1) >> c_p(p+p_1)$, τ_t can be simplified to $\tau_t \approx [c_n(n+n_1)]^{-1}$. The analytical expression of the current noise spectral density of this structure at low frequencies becomes then

$$S_I(f \to 0) \approx \frac{4I^2}{LAn^2} \frac{n_1 n_t}{c_n (n+n_1)^2} \tag{5.21}$$

The g-r noise of the n^+-n-n^+ bulk resistor with the defect trap center described above is simulated and plotted as a function of frequency in Fig. 5-2 and compared with the analytical g-r noise expression (5.19). The simulated noise is in excellent agreement with the theory. The simulated bulk g-r noise rolls off at the calculated corner frequency $f_c = 1/2\pi\tau_t \approx 3$ MHz, and has a slope of $1/f^2$ beyond f_c.

G-r noise simulations as a function of bias are shown in Fig. 5-3. Under low bias conditions, the g-r noise is below the velocity fluctuation noise. The simulation is in good agreement with the analytical expressions (5.19) and (5.21) under low bias conditions. When the bias increases, the magnitude of the simulated g-r noise emerges from the velocity fluctuation noise, reaches a peak and then starts to decrease due to predominantly space-charge injection from the n^+ drain region of the device. The space charge injection as a function of bias is illustrated in Fig. 5-4. Due to the injection, injected electrons fill the traps with a doping density of 10^{12} cm^{-3} as shown in Fig. 5-5 and subsequently the electron Fermi level in the n-region moves away from the trap energy level. As a result the g-r mechanism at that level becomes less effective due to a decrease in the recombination rate and, via detailed balance, generation rate. The result is then a decrease of the local g-r noise strength.

The scalar Green's function can be derived from (5.20) analytically, as

$$S_I = \frac{I^2}{N^2} S_{\Delta N_t} = \int_{vol} |\tilde{G}\tilde{G}^*| K_{\gamma_t,\gamma_t} \Delta v \tag{5.22}$$

Under low bias condition where N is independent of bias, the Green's function is proportional to I. Under high bias conditions, N increases with bias as the carrier injection into the n-region becomes significant. As a result the Green's function becomes less bias dependent, as shown in Fig. 5-6. The same trend can be seen in the distributed current spectral density, shown in Fig. 5-7.

5.4 Discussion

Fig. 5-3 shows that for the trap example selected the g-r noise dominates the velocity fluctuation noise over a wide bias range, hence the chosen trap density of 10^{12} cm^{-3} clearly exceeds the maximum allowable defect density N_{Tmax} for g-r noise free operation. The value of N_{Tmax} for this particular trap follows from equating the g-r noise magnitude with the magnitude of the velocity fluctuation noise component. Under low bias conditions in the ohmic regime, the quantity of N_{Tmax} can be derived analytically by setting (5.21) equal to $S_{I\Delta v} = 4kT/R$. Thus

$$N_{Tmax} = \frac{kTL^2}{q\mu V^2} \frac{c_n (n+n_1)^3}{n_1} \tag{5.23}$$

with the assumptions that $n_t \approx c_n n N_t \tau_t$ and $\tau_t \approx [c_n (n+n_1)]^{-1}$. Simulations were carried out by varying the value of N_T to obtain a g-r noise level equal to the velocity fluctuation noise level as a function of trap energy level for a bias of 0.1V at room temperature with the c_n and c_p values previously specified. The simulation results are presented in Fig. 5-8 and agree with the low bias predictions of (5.25). The figure shows that defect levels close to the Fermi level at $E_C - E_F$ = 0.265 eV require stricter constraints than defect levels further away from E_F, corroborating the fact that traps at the Fermi level produce g-r noise more effectively. Fig. 5-8 also shows that at higher bias lower defect densities are required for g-r noise free operation primarily due to an increase in magnitude of the Green's function with bias. To estimate N_{Tmax} at high bias for a trap at the Fermi level, the worst case scenario, we use n_1 = n and n_t = 0.5 N_T. Upon substituting these assumptions in (5.17) and integrating over device volume, the low frequency plateau value of the number spectral density becomes

$$S_{\Delta N}(0) = \frac{N_T A L}{2 c_n n} \tag{5.24}$$

The value of $S_{\Delta N}(0)$ via (5.22) needs to be compared with the magnitude of the velocity fluctuation noise $S_{I\Delta v}$ component as read from the simulated data presented in Fig. 5-3. Note that I, N, and $S_{I\Delta v}$ are affected by carrier heating and space charge injection. The value of I follows from the simulated I-V characteristic presented in Fig. 5-9, whereas N follows from

$$N = \frac{CV}{q} + N_d AL \tag{5.25}$$

where $C = 1.7C_o$ with C_o representing the geometrical capacitance of the device. Eq. (5.25) is based on early work by Lampert and Mark [27] and was later confirmed by Bosman *et al.* [28]. Values of N thus calculated agree well with simulated values presented in Fig. 5-4. The value of N_{Tmax} can now be calculated from

$$N_{Tmax} = 2\frac{c_n N^3 S_{I\Delta v}(0)}{(ALI)^2} \tag{5.26}$$

resulting in $N_{Tmax} = 1.4 \cdot 10^{11}$ cm^{-3} at 2 V and $2 \cdot 10^{11}$ cm^{-3} at 4 V, respectively, in very good agreement with the simulated data presented in Fig. 5-8.

5.5 Conclusions

A detailed comparison of simulated and analytical noise predictions shows that the maximum allowable defect density for g-r noise free operation of two terminal bulk devices can accurately be estimated even in the presence of hot carrier effects and space charge injection. In addition the noise simulations reveal that the g-r noise plateau value of a specific trap reaches a maximum as a function of bias and subsequently decreases with increasing bias due to space charge injection and carrier heating to levels below the velocity fluctuation noise.

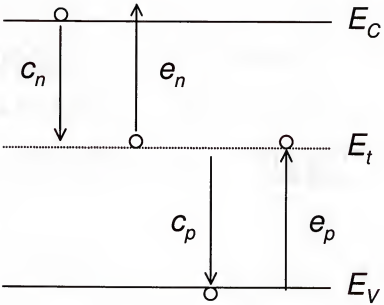

Figure 5-1. Carrier transitions between the continuum states and localized defect states

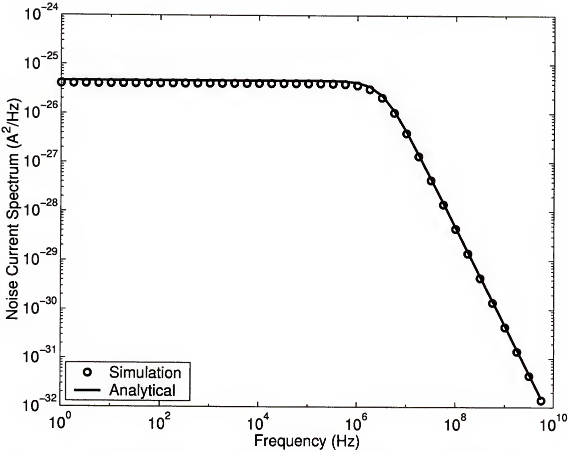

Figure 5-2. Comparison between the simulated and analytical current noise spectral density as a function of frequency. The bias across the device is set to 0.1 V

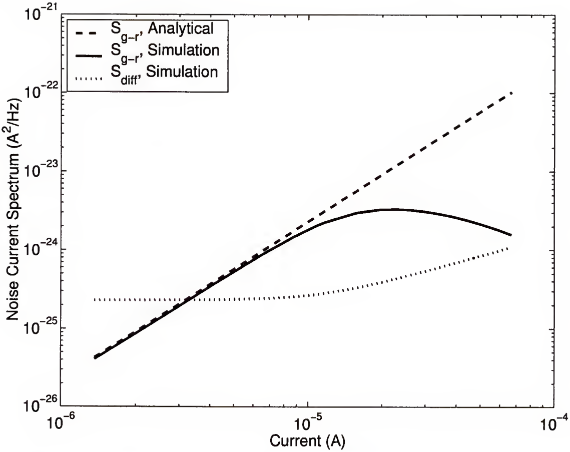

Figure 5-3. Comparison between the simulated and analytical g-r current noise spectral density (f = 1 Hz) as a function of the bias voltage. The dashed line represents the analytical expression (5.21). The solid line is the simulated g-r noise. The dotted line is the simulated velocity fluctuation noise.

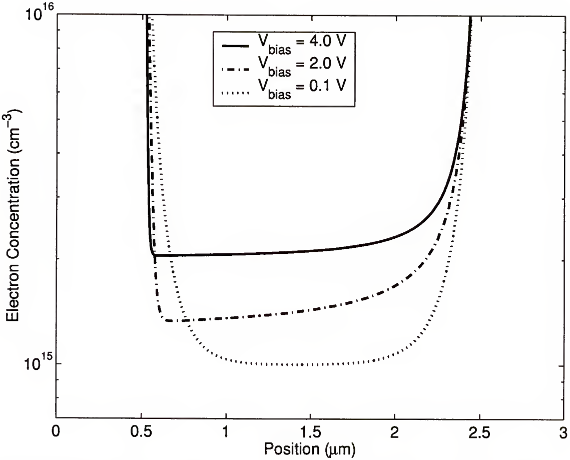

Figure 5-4. Electron concentration n in the n-region as a function of position under different bias conditions. Under the low bias condition (V_{bias} = 0.1 V), $n \approx N_d$. As the bias increases (V_{bias} > 1.0 V), $n > N_d$.

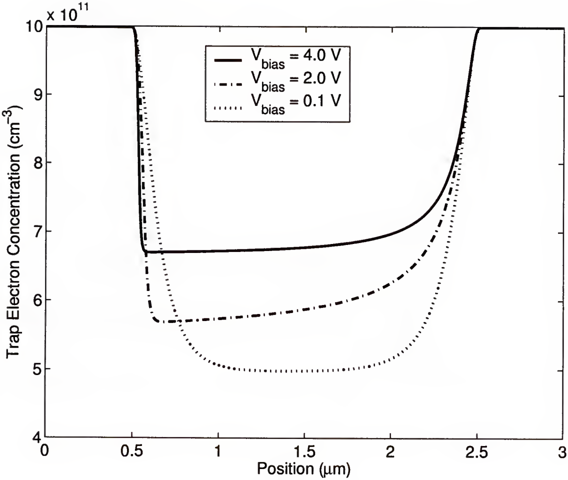

Figure 5-5. Trap electron concentration n_t as a function of position under different bias conditions

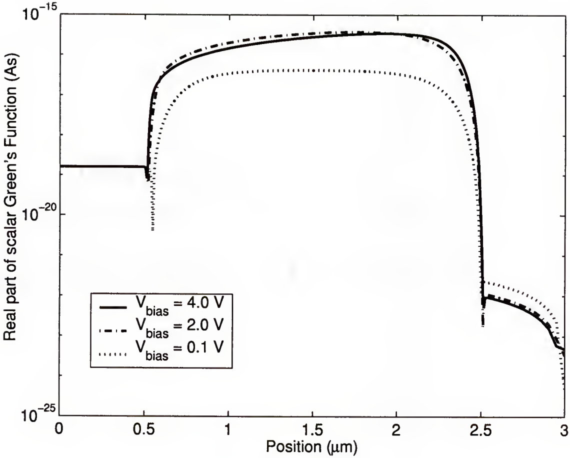

Figure 5-6. Scalar Green's function under different bias conditions

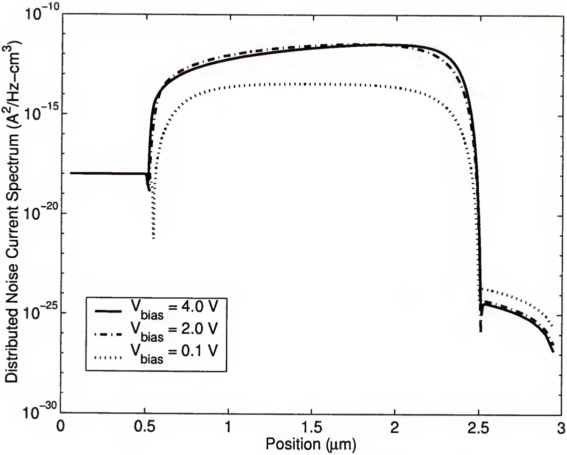

Figure 5-7. Distributed current noise spectral density under different bias conditions

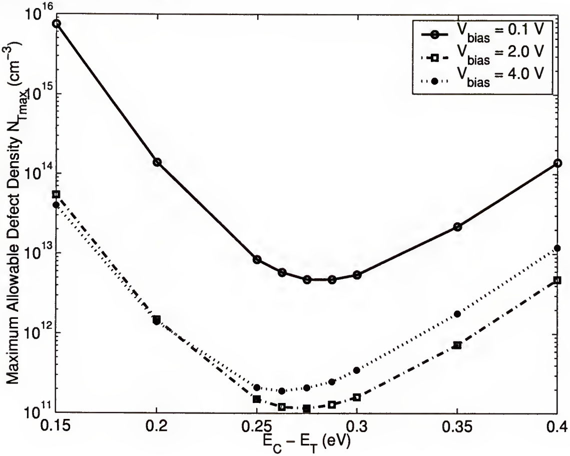

Figure 5-8. Defect density N_{Tmax} as a function of defect energy under different bias conditions

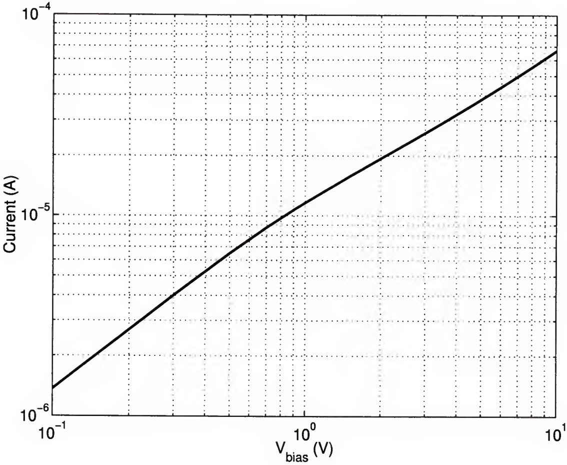

Figure 5-9. I-V characteristic

CHAPTER 6
CONCLUSION AND SUGGESTIONS FOR FUTURE RESEARCH

The velocity fluctuation noise, the bulk and interface generation-recombination (g-r) noise, and the oxide trapping noise mechanisms were implemented into FLOODS. Each has been verified with its known analytical expressions to validate its accuracy. By matching the simulation with the measured noise data of the device, this simulation tool can become useful for probing the defect density distributions in both the silicon bulk and oxide regions.

One suggestion for future research is to utilize the noise simulation tool to study the noise in advance VLSI devices, such as silicon-on-insulator (SOI) MOS transistors. The carrier tunneling mechanism that produces the $1/f$ noise in MOS devices, as the author has demonstrated, also exists in SOI devices. It is possible that the oxide trapping noise is more critical for SOI devices than for MOS devices, since they have more silicon-oxide interface area. In addition, since the carrier tunneling is not limited by the device size, the oxide trapping noise simulation can also be used to analyze the low-frequency noise in short-channel ($L < 0.4$ μm) MOS transistors.

As both the length and the width of the MOS devices become smaller, single defects in the oxide may become important. Instead of getting a $1/f$-like noise spectrum, the simulated outcome would consist of a limited numbers of Lorentzian spectra, and show Random Telegraph Signal (RTS) noise in the time domain. Since the noise simulation tool is capable of accepting discrete defect density distributions, it can be used to study and simulate the RTS noise.

Another suggestion is to combine the oxide trapping noise with the harmonic balance simulation, to simulate the $1/f$ noise sidebands observed in the mixers and voltage controlled oscillator (VCO) circuits.

Finally, another interesting topic would be to use the oxide trapping noise simulator to investigate the mobility fluctuation noise. As the carriers tunnel between the traps in the oxide and at the interface, the perpendicular field at the channel would fluctuate (due to the charging and discharging of the trap centers as the carriers tunneling in and out). This indirectly modulates both the carrier mobility and current density in the channel. Preliminary simulation results have shown that this phenomenon can be captured by the noise simulation tool. More research is currently underway to study this phenomenon.

REFERENCES

[1] F. N. Hooge, "$1/f$ noise is no surface effect," *Physics Letters*, vol. 29A, pp. 139–140, Apr. 1969. 2

[2] F.-C. Hou, G. Bosman, E. Simoen, J. Vanhellemont, and C. Claeys, "Bulk defect induced low-frequency noise in n^+-p silicon diodes," *IEEE Trans. Electron Devices*, vol. 45, pp. 2528–2536, Dec. 1998. 2

[3] A. L. McWhorter, "$1/f$ noise and germanium surface properties," in *Semiconductor Surface Physics* (R. H. Kingston, ed.), pp. 207–228, Philadelphia: University of Pennsylvania Press, 1957. 2, 63

[4] F. Bonani, G. Ghione, M. R. Pinto, and R. K. Smith, "An efficient approach to noise analysis through multidimensional physics-based models," *IEEE Trans. Electron Devices*, vol. 45, pp. 261–269, Jan. 1998. 3, 4, 7, 93, 94

[5] F. Bonani and G. Ghione, "Generation-recombination noise modeling in semiconductor devices through population or approximate equivalent current density fluctuations," *Solid-St. Electron.*, vol. 43, pp. 285–295, 1999. 3, 31

[6] F.-C. Hou, G. Bosman, and M. E. Law, "Characterization of generation-recombination noise using a physics-based device noise simulator," in *Proc. 15th Int. Conf. Noise Phys. Syst. 1/f Fluct.* (C. Surya, ed.), pp. 35–38, London: Benthom Press, 1999. 3, 94, 95

[7] J. E. Sanchez, F.-C. Hou, G. Bosman, and M. E. Law, "Physics based noise simulation implemented in FLOODS," in *TECHON 98*, Semiconductor Research Corporation, 1998. 3

[8] W. Shockley, J. A. Copeland, and R. P. James, "The impedance field method of noise calculation in active semiconductor devices," in *Quantum Theory of Atoms, Molecules, and the Solid-State* (P.-O. Lowdin, ed.), NY: Academic, 1966. 4

[9] F. H. Branin, "Network sensitivity and noise analysis simplified," *IEEE Trans. Circuit Theory*, vol. CT-20, pp. 285–288, May 1973. 4

[10] J.-P. Nougier, "Fluctuations and noise of hot carriers in semiconductor materials and devices," *IEEE Trans. Electron Devices*, vol. 41, pp. 2034–2049, Nov. 1994. 5

[11] K. M. van Vliet, "Noise and admittance of the generation-recombination current involving SRH centers in the space-charge region of junction devices," *IEEE*

Trans. Electron Devices, vol. ED-23, pp. 1236–1246, Nov. 1976. 26, 30, 31, 93, 94

[12] A. van der Ziel, *Noise in Solid State Devices and Circuits*. NY: Wiley, 1986. 31, 94

[13] G. Bosman and J. J. Zijlstra, "Generation-recombination noise in p-type silicon," *Solid-St. Electron.*, vol. 25, pp. 273–280, 1982. 34

[14] Z. Celik-Butler and T. Y. Hsiang, "Spectral dependence of $1/f^{\gamma}$ noise on gate bias in n-MOSFETs," *Solid-St. Electron.*, vol. 30, no. 4, pp. 419–423, 1987. viii, 49, 54, 56, 65, 67, 68, 70, 73

[15] S. Christensson, I. Lundström, and C. Svensson, "Low frequency noise in MOS transistors–I Theory," *Solid-St. Electron.*, vol. 11, pp. 797–812, 1968. 51, 63, 64, 65, 66, 67

[16] S. T. Hsu, D. J. Fitzgerald, and A. S. Grove, "Surface-state related $1/f$ noise in p-n junctions and MOS transistor," *Applied Physics Letters*, vol. 12, pp. 287–289, May 1968. 63

[17] H.-S. Fu and C.-T. Sah, "Theory and experiments on surface $1/f$ noise," *IEEE Trans. Electron Devices*, vol. ED-19, pp. 273–285, Feb. 1972. 63, 64, 65

[18] Z. Celik and T. Y. Hsiang, "Study of $1/f$ noise in n-MOSFET's: Linear region," *IEEE Trans. Electron Devices*, vol. ED-32, pp. 2797–2802, Dec. 1985. 63, 65, 71, 73

[19] M. Liang and M. E. Law, "Influence of lattice self-heating and hot-carrier transport on device performance," *IEEE Trans. Electron Devices*, vol. 41, pp. 2391–2398, Dec. 1994. 64

[20] M. Liang and M. E. Law, "An object oriented approach to device simulation," *IEEE Trans. Computer-Aided Design*, vol. 13, pp. 1235–1240, Oct. 1994. 64

[21] E. Burstein and S. Lundquist, *Tunneling Phenomena in Solids*. NY: Plenum, 1969. 64, 67

[22] M. Schulz, "Interface states at the SiO_2-Si interface," *Surface Science*, vol. 132, pp. 422–455, 1983. 65

[23] C. T. Sah, "Theory of low-frequency generation noise in junction-gate field-effect transistors," *Proc. IEEE*, vol. 52, pp. 795–814, July 1964. 65

[24] F. P. Heiman and G. Warfield, "The effects of oxide traps on the MOS capacitance," *IEEE Trans. Electron Devices*, vol. ED-12, pp. 167–178, Apr. 1965. 67

[25] W.-C. Lee and C. Hu, "Modeling gate and substrate currents due to conduction- and valence-band electron and hole tunneling," in *2000 Symposium on VLSI Technology, Digest of Technical Papers*, pp. 198–199, 2000. 69

[26] G. Bosman, "Charge transport and device parameters from noise measurements," *Special issue on Fluctuation Phenomena in Electronic and Photonic Devices, IEEE Trans. Electron Devices*, vol. ED41, pp. 2198–2204, 1994. 91

[27] M. A. Lampert and P. Mark, *Current Injection in Solids.* NY: Academic Press, 1970. 98

[28] G. Bosman, J. J. Zijlstra, and F. Nava, "The longitudinal diffusion coefficient and mobility of hot electrons in silicon," *Solid-St. Electron.*, vol. 24, pp. 5–9, 1981. 98

BIOGRAPHICAL SKETCH

Fan-Chi (Frank) Hou received the degree of Bachelor of Science in Electrical Engineering, with honors, from the University of Florida (UF) in December 1993. He has been a graduate research assistant in the Noise Research Laboratory at UF since January 1995, and received his Master of Science in Electrical and Computer Engineering in August 1996. Since then he has been pursuing his PhD. His research interests have focused on noise-related phenomena in semiconductor devices. He is a member of *Eta Kappa Nu*, *Tau Beta Pi*, and the *IEEE.*

I certify that I have read this study and that in my opinion it conforms to acceptable standards of scholarly presentation and is fully adequate, in scope and quality, as a dissertation for the degree of Doctor of Philosophy.

Gijs Bosman, Chair
Professor of Electrical and
Computer Engineering

I certify that I have read this study and that in my opinion it conforms to acceptable standards of scholarly presentation and is fully adequate, in scope and quality, as a dissertation for the degree of Doctor of Philosophy.

Mark E Law

Mark E. Law
Professor of Electrical and Computer
Engineering

I certify that I have read this study and that in my opinion it conforms to acceptable standards of scholarly presentation and is fully adequate, in scope and quality, as a dissertation for the degree of Doctor of Philosophy.

Kenneth

Kenneth K. O
Professor of Electrical and Computer
Engineering

I certify that I have read this study and that in my opinion it conforms to acceptable standards of scholarly presentation and is fully adequate, in scope and quality, as a dissertation for the degree of Doctor of Philosophy.

Robert M Fox

Robert M. Fox
Associate Professor of Electrical and
Computer Engineering

I certify that I have read this study and that in my opinion it conforms to acceptable standards of scholarly presentation and is fully adequate, in scope and quality, as a dissertation for the degree of Doctor of Philosophy.

Christopher J. Stanton

Christopher J. Stanton
Professor of Physics

This dissertation was submitted to the Graduate Faculty of the College of Engineering and to the Graduate School and was accepted as partial fulfillment of the requirements for the degree of Doctor of Philosophy.

May 2002

Pramod P. Khargonekar
Dean, College of Engineering

Winfred M. Phillips
Dean, Graduate School